

Universität Stuttgart
5. Physikalisches Institut

Master's Thesis

INTERFACING SINGLE PHOTONS WITH ALKALI VAPOURS

submitted on 9 May 2018

Author:
Lea Kopf

Supervisor:
Dr. Robert Löw

Main Examiner:
Prof. Dr. Tilman Pfau

Second Examiner:
Prof. Dr. Jörg Wrachtrup

Abstract

Reliable, applicable, and efficient quantum memories are missing components for large-scale quantum networks. This work paves the way for future single-photon storage protocols in caesium vapours. As part of this thesis a new experimental laser system has been set up which meets various requirements for future storage protocols in a electromagnetically induced transparency scheme. Its functionality is proven in electromagnetically induced transparency and pulse deformation measurements.

Zusammenfassung

Die Quantenkommunikation ist ein vielversprechendes anwendungsbezogenes Gebiet der Quanteninformatik. Hierbei werden Quantenzustände über eigens dafür vorgesehene Netzwerke übertragen. Diese Quantennetzwerke ermöglichen über verschränkte Zustände und Quantenschlüsselaustausche absolut abhörsichere Kommunikation. Um Verluste in großflächigen Quantennetzwerken auszugleichen, sind sogenannte Quantenrepeater nötig. Diese sind auf zuverlässige, wartungsarme und effiziente Quantenspeicher angewiesen. Diese Arbeit beschäftigt sich mit der Realisierung eines Quantenspeichers in warmen Alkalidämpfen. Sie bieten sich für einen großflächigen, wartungsarmen Ausbau an, da sie bei Raumtemperatur und nicht unter Hochvakuum arbeiten und somit robust sind und eine anspruchslose Anlage benötigen. Darüber hinaus sind sie leicht auf Chips implementierbar und somit für die Massenproduktion geeignet.

In dieser Arbeit wurde ein Versuchsaufbau für zukünftige Speicherprozesse erstellt. Der Aufbau erfüllt die Anforderungen eines Quantenspeichers basierend auf einem Speichervorgang mit einem elektromagnetisch induzierten Transparenz (EIT) Schemas. Der Versuchsaufbau schließt zwei Lasersysteme, eine zeitabhängige Kontrolle der Lichtfelder und ein Filter- und Detektiersystem mit ein.

Die Funktionalität des Setups wird mit EIT und Pulsdeformationsmessungen nachgewiesen. Bei den EIT-Messungen wurde zwischen gleich- und gegenläufigen Lichtstrahlen unterschieden. Mit gleichläufigen Strahlengängen konnten Transparenzfenster mit bis zu 275 MHz Halbwertsbreite und simulierten Gruppenverzögerungen von über $3 \cdot 10^{-24}$ s gemessen werden. Mit gegenläufigen Strahlen konnte ein fast 400 MHz breites Transparenzfenster mit Verzögerungen über $2 \cdot 10^{-25}$ s gemessen werden. Die Pulsdeformationsmessungen stimmen mit der Simulation größtenteils überein, sind jedoch durch die begrenzte Auflösung der Messelektronik limitiert und durch Hintergrundprozesse überlagert.

In einer weiterführenden Arbeit soll das System mit einem „Extended Lambda“-Schema vertieft werden. Diese und weitere Verbesserungen des Aufbaus werden Einzelphotonenspeicherprozesse ermöglichen.

Eigenständigkeitserklärung

Hiermit versichere ich,

1. dass ich die Arbeit selbständig verfasst habe,
2. dass ich keine anderen als die angegebenen Quellen benutzt und alle wörtlich oder sinngemäß aus anderen Werken übernommenen Aussagen als solche gekennzeichnet habe,
3. dass die eingereichte Arbeit weder vollständig noch in wesentlichen Teilen Gegenstand eines anderen Prüfungsverfahrens gewesen ist, und
4. dass das elektronische Exemplar mit den anderen Exemplaren übereinstimmt.

Stuttgart, 10. Mai 2018

Lea Kopf

Contents

1	Introduction	1
1.1	Quantum networks and quantum memories	1
1.2	This work	2
2	Motivation	3
2.1	Quantum networks	3
2.2	Overview of quantum memory schemes	5
3	Atomic physics in hot alkali vapours	7
3.1	Physical properties of caesium	7
3.2	Interaction of atoms with light	8
3.2.1	Susceptibility and refractive index	8
3.2.2	Two-level system	9
3.2.3	Three-level system	13
3.3	Basic principle of the EIT storage scheme	18
3.3.1	Limitations	21
3.4	Spectroscopy	24
3.4.1	Optical density	24
3.4.2	Broadening mechanisms	25
4	Experimental setup	28
4.1	Self-built diode laser	28
4.1.1	Fabry-Pérot cavity and mode hopping	30
4.2	DL Pro laser system	31
4.3	Laser lock system	31
4.4	Electro-optical modulator - EOM	32
4.5	Tapered amplifier - TA	34
4.5.1	Shaping the output beam	36
4.6	Vapour cells	36
4.6.1	Cell mount	36
4.6.2	Glass cell design	37
5	Measurements	41
5.1	Co-propagating EIT scheme	41
5.2	Counter-propagating EIT scheme	43
5.3	Pulse deformation	46

6 Outlook	50
6.1 The lambda scheme	50
6.2 The extended lambda scheme	51
7 Summary and conclusion	53
8 Acknowledgement	54
List of References	55
List of Figures	58

1 Introduction

Quantum mechanics seems to be inapprehensible and defies the logical comprehension of our classical experiences. Locality, causality, and continuity are abolished. Today, the surprising effects can be harnessed in a diverse range of applications.

The band structure of semiconductor electronics are exploited in smart phones and laptops. Lasers enable telecommunication through fibre optics. Atomic clocks are needed for reliable global positioning systems. MRI imaging is widely-used for medical diagnostics. Quantum computation and communication have great potential to further exhaust quantum mechanics in our future modern world [NC10].

In 2000 the DiVincenzo criteria, a list of five requirements for quantum computing and two requirements for quantum communication, were published in “The Physical Implementation of Quantum Computing” [DiV00]. It is considered a milestone in the scientific development of quantum computing and communication.

1.1 Quantum networks and quantum memories

In the modern world, information and communication networks play a major role. Exchanging confidential information in a secure and fast manner over long distances is not only indispensable for international business and financial purposes, but is recently finding its way into personal life. Online social networks enjoy great popularity. Today’s world without online media is unimaginable. The demand for secure communication insuring protection of data privacy is rapidly rising. The political interest in the prevention of foreign surveillance through intelligent corps promote research and development. Pioneers from industry like *Toshiba*, *Huawei*, and *Hewlett-Packard* have discovered the value lying in secure quantum communication and invest in research and development. The companies *ID Quantique SA*, *MagiQ Technologies*, and *SeQureNet* already offer products implementing the Quantum Key Distribution - a protocol which exchanges a cryptographic key to decode messages sent over insecure classical channels.

Quantum networks use the information transfer through entangled qubits. They are main components of quantum computation, cryptography, and communication schemes. Information transfer through entangled qubits exploit their quantum mechanical properties. Since their quantum state is dependent on the state of its counterpart, knowledge over one quantum state consequently leads to the knowledge of the other. According to the

no-cloning theorem these quantum states can not be duplicated hence, making network attacks on quantum networks easy to detect.

Photonic implementations are suitable, since single photons have weak interactions with their surrounding and are easily manipulated by well-known optical elements. Due to the overall low transmission efficiencies and reliability over long distances, real world implementations of large-scale quantum networks are challenging. The efficiency is limited by the complicated creation of on-demand entangled photons and losses through communication channels. In classical networks signal losses are compensated through an amplification of the signal. Classical amplification is however forbidden by the no-cloning theorem. Quantum repeaters have the potential of increasing the distance over which entangled photons can be transmitted. More details concerning quantum communication networks are presented in chapter 2.

Quantum memories are a crucial part of quantum repeaters. Quantum memories implemented in ring cavities, in single ions, in solid states or in cold atoms are currently investigated by the research community. However, high vulnerability, expensive mass production or the overall complexity make them undesirable for large-scale quantum communication in which quantum repeaters need to be located in physically remote places with low-level maintenance.

1.2 This work

Room-temperature quantum memories in alkali vapours are appropriate vessels for devices which are robust and easy to implement on a chip with broad bandwidth capabilities. This thesis lays the groundwork of the realisation of feasible room-temperature quantum memories in caesium vapours through electromagnetically induced transparency schemes - short EIT schemes.

The theoretical framework concerning the atomic physics in hot alkali vapour cells and the EIT scheme is provided in chapter 3. Chapter 4 presents the experimental setup with which various requirements for future storage protocols are met. Chapter 5 summarizes the measurements done to demonstrate the functionality of the setup and characterizes the first properties of the EIT scheme. In chapter 6 the envisioned improvements for realising single-photon storage protocols are reviewed.

2 Motivation

Quantum communication is a promising field of quantum technology which enjoys great interest not only in the scientific community but also in High-Tech industrial branches. It allows secure communication through information transfer through entangled photons and Quantum Key Distribution schemes. Products by *ID Quantique SA*, *MagiQ Technologies*, and *SeQureNet* lead the way towards applicable quantum communication networks.

Building a reliable network in which entanglement is distributed between nodes over large distances is challenging the current research community. Highly efficient, reliable, and feasible quantum memories are needed for its implementation. This work lays the framework for the realisation of a room temperature, robust, and easy to operate quantum memory. This chapter outlines the motivation for approaching quantum memories in alkali vapour cells.

2.1 Quantum networks

Photonic quantum networks promise to overcome classical thresholds of state-of-the-art technologies. Quantum communication, computation, cryptography, and metrology will profit from highly efficient quantum networks. Classical communication technologies transfer information through electron carriers. Photons, which do not interact as strong with their surrounding as classical information carriers, need significantly less enhancement over long distances. Furthermore, photons can transfer more information through their quantum mechanical state than the classical binary bits.

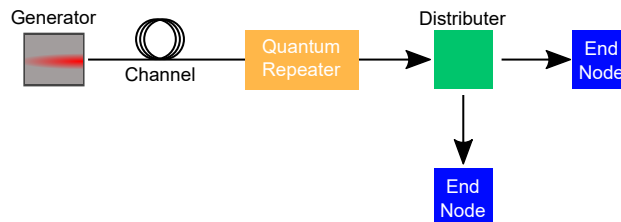


Figure 2.1: Basic components of quantum networks. A photon is generated, sent through a channel, “amplified” in a quantum repeater and distributed to the end nodes where they are processed [Kim08].

Figure 2.1 illustrates the principle of quantum networks. The simplest network consist of three main components: a qubit generator, communication channels, and end nodes [Kim08]. The information is generated and then transferred over communication channels to the end nodes, where they are read out. In addition, quantum channels by distributing qubits to differing end nodes will further improve the capacity of the infrastructure. The distance over which photons can be sent is limited by losses and decoherence in the photonic channels [DLCZ01]. Current optical glass fibres have a loss of 0.2 dB/km at the telecom wavelength around 1550 nm. This means that 50% of the signal gets lost after a passage of 15 km. In classical long distance networks the losses are compensated by signal amplifiers.

Quantum repeaters have the potential to increasing the distance over which photons can be sent. However, the no-cloning theorem forbids the reproduction of quantum mechanical states. The Duan-Lukin-Cirac-Zoller (DLCZ) protocol [DLCZ01] [LST09] theoretically describes the realisation of quantum repeaters without quantum memories. The principle of quantum repeaters is based on entanglement swapping and on local operations and classical communication (LOCC).

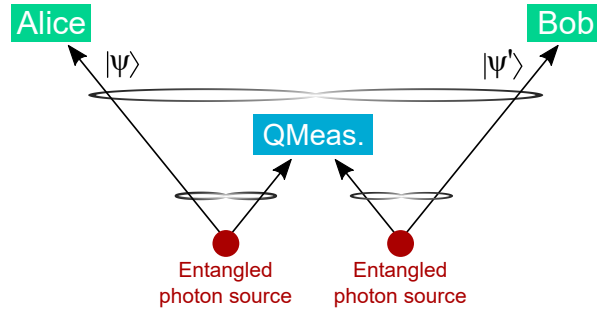


Figure 2.2: Entanglement swapping scheme as described in [ZZHE93]. “QMeas.” is the abbreviation for quantum measurement.

- The entanglement swapping scheme is shown in figure 2.2. Two sources create an entangled photon pair. A joined quantum measurement on one photon per pair defines their resemblance [ZZHE93]. If both photons are in the same state, the not measured photons are entangled. If the photons do not share the same state they are sorted out by post-selection. With this scheme, the entanglement can be distributed over larger distances compared to an entangled photon pair generated in a single source.
- LOCC schemes are not dependent on sharing entanglement over classical communication channels and thus, are not limited by their losses and decoherences [CLM⁺14]. In a simple picture it can be described by two observers Alice and Bob who share a state which can be one of the two possible Bell states. Alice and Bob perform a measurement on their state and compare it by exchanging the outcome of their measurement through a classical channel. This way the state is defined.

Quantum memories are an additional component of the quantum communication toolbox further increasing the distances achievable between nodes.

Frequency conversion

The current communication infrastructure is mostly based on the telecom wavelength at 1550 nm due to the low absorption of glass at this wavelength. Therefore, the optical components such as glass fibres are designed for the telecom wavelength in modern networks. It is useful to be unrestricted to the telecom wavelength in the creation of entangled photon pairs to be able to use a wider range of creation schemes. Through frequency conversion, single photons created at a different wavelength can be converted to the telecom wavelength [BEK⁺17] and still use the resent glass fibre infrastructure. This will further decrease the effort and price needed for implementing a secure quantum network.

2.2 Overview of quantum memory schemes

Since the creation of entangled photon pairs through commonly used methods such as the spontaneous parametric down-conversion is a probabilistic method, it is difficult to create two entangled photon pairs simultaneously. For joined quantum state measurements, it is thus necessary to store the early-arriving photon until the late-arriving photon is created. These storage schemes are implemented by quantum memories as discussed in this section. For further reading, [LST09] gives an overview of the most commonly used methods to implement a quantum memory.

Delay lines

Delay lines provide a simple, well-understood method to delay single photons. They are commonly used in quantum photonics. The quantum dot community uses them for Hong-Ou-Mandel measurements, for example. In most cases, delay lines consist of a common optical fibre whose length defines a fixed delay. The drawback is that the photon cannot be read out on demand and delays require a well-known process. Furthermore, for longer delays losses increase. Delay lines provide a storage half-time of about 70 μ s [LST09] at the telecom wavelength. After that time the photons can be considered lost.

Ring cavity

Ring cavities as in [KXCK17] store photons in a cavity. A switchable component changes the polarization of the stored photons. This is used as an on-demand output of the cavity. The setup of [KXCK17] is schematically depicted in figure 2.3. Incoming photons are stored in the cavity by being reflected at the beam splitter. They leave the cavity after their polarization is changed by a high-speed Pockels cell allowing their escape by transmitting through the beam splitter. The read-out is limited by the cycle time and the response time of the Pockels cell.

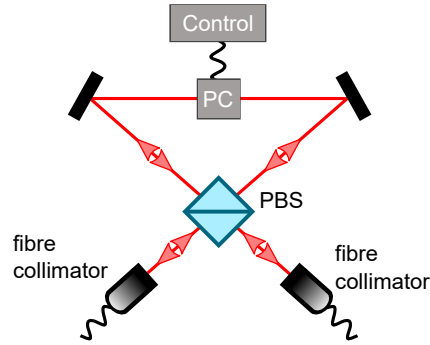


Figure 2.3: Scheme of the ring cavity introduced in [KXCK17]. Incoming photons are stored in the cavity until the polarization is switched by the Pockels cell (PC) allowing the transmittance through the polarizing beam splitter (PBS).

Cold atoms

Implementations of quantum memories in cold atoms use the same principles as the realisation in hot vapour. However, they do not have to deal with noise channels and broadening mechanisms introduced by temperature, which are discussed in section 3.4.2. On the other hand, the setup is expensive, cannot be implemented on a chip and is not suitable for remote places with low-level maintenance. Delays of around 1 ms were implemented with sodium atoms cooled to $0.9 \mu\text{K}$ [LDBH01].

Hot alkali vapours

The advantage of quantum memories in hot vapours is their feasibility and robustness. Hot alkali vapours do not need cooling apparatuses or high vacuum such as quantum memories in cold atoms. They can be miniaturised and implemented on chips. EIT-based schemes and memories based on photon echos have recently been realised. Through the potential of mass production they are affordable in large scale networks. Storage times for single photons of some hundred nanoseconds [Rei11] [WBH⁺17] and a coherence lifetime of 2.7 ms with a four-wave mixing scheme in a continuous write field [SEDF17] have been achieved, recently.

Further schemes in atomic and solid state systems [LFSM05] such as the off-resonant Faraday interaction [JSC⁺04] or photon echos [HHS⁺08] through controlled reversible inhomogeneous broadening (CRIB) [ALSM06] or frequency combs [AUA⁺10] are not discussed in this thesis. The EIT storage scheme which is the main focus of this thesis, is presented in section 3.3 in detail.

3 Atomic physics in hot alkali vapours

The interaction of light with atoms provides the opportunity to control photons. Light-atom interaction in cold environments offer well-understood processes due to low interaction with external forces. However, their complex cooling mechanisms and expensive setups render cold atomic ensembles unsuitable for robust and reproducible applications. On the other hand, atomic vapours at room-temperature provide a simplified medium where the light propagation can be manipulated. A good understanding of the processes is indispensable for reliable quantum memory protocols with a high read-out efficiency.

The experiments presented in this thesis were done in caesium vapour cells. Their resemblance to hydrogen atoms makes them easy to describe and convenient to work with. The theoretical background of the element, the atom-light interaction, the basic principle of the EIT storage scheme and spectroscopic measurement principles are introduced in this chapter.

3.1 Physical properties of caesium

Caesium is a stable highly reactive alkali element. Alkali metals are atoms with only one valence electron hence hydrogen-like and easy to describe. Table 3.1 gives a short overview of the physical properties of the caesium 133 isotope, the only stable isotope of caesium. The hyperfine splitting of the ground state $6^2S_{1/2}$ of 9.192 GHz (as depicted by figure 3.1) is large compared to other alkali elements. This property makes it a suitable choice for EIT experiments.

	Abbreviation	Value	Transition
Atomic Number	Z	55	
Total Nucleons	$Z + N$	133	
Atomic Mass	m	$2.207 \cdot 10^{-25}$ kg	
Melting Point	T_M	28.44°C	
Boiling Point	T_B	671°C	
Lifetime	τ	34.894 ns	$6^2S_{1/2} \rightarrow 6^2P_{1/2}$
Decay Rate	Γ	$2\pi \cdot 4.5612$ MHz	$6^2S_{1/2} \rightarrow 6^2P_{1/2}$

Table 3.1: Physical properties of caesium-133. The values are introduced in [Ste10].

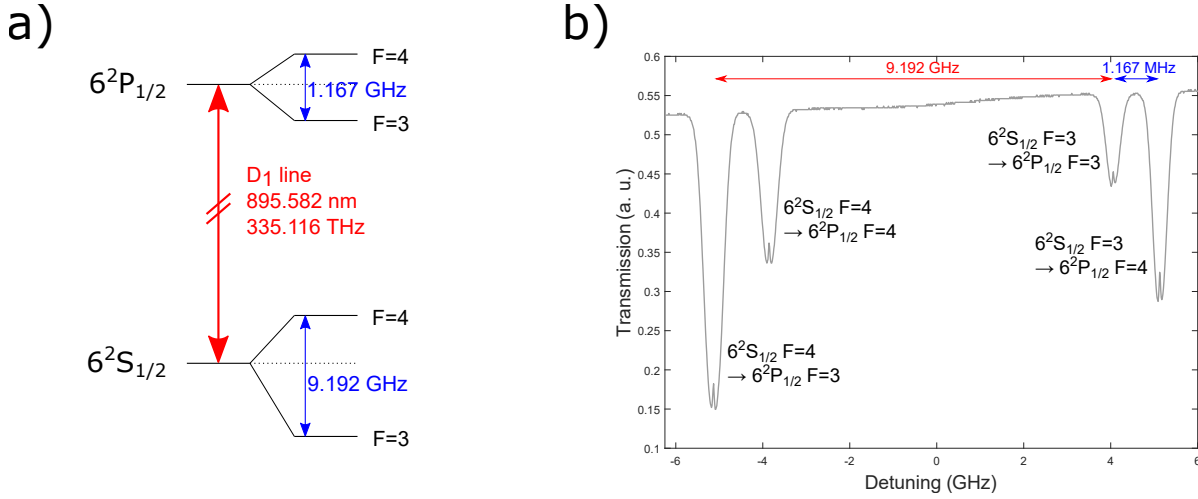


Figure 3.1: a) Energy levels of the caesium D₁ transition. b) The corresponding spectrum with lamb dips. The values are from [Ste10].

3.2 Interaction of atoms with light

The basics of the atom-light interaction have been extensively studied in educational literature. This section only gives an overview highlighting the topics needed in this thesis.

3.2.1 Susceptibility and refractive index

The susceptibility χ is defined as $\chi = \chi' + i\chi''$ with the real part χ' and its imaginary part χ'' [ST08]. The wavevector can be written as $k = k_0\sqrt{1 + \chi}$. Dividing it in real and imaginary part yields

$$k = k_0\sqrt{1 + \chi} = \beta - i\frac{1}{2}\alpha \quad (3.1)$$

in which α describes the absorption and β the phase propagation. By defining the refractive index n , β can be written as $\beta = nk_0$.

Alkali vapours are in the regime of a weak absorbing medium, i.e. $\chi'' \ll 1 + \chi'$. We get $\sqrt{1 + \chi' + i\chi''} \approx \sqrt{1 + \chi'}(1 + i\frac{1}{2}\delta)$ with $\delta = \chi''/(1 + \chi')$. With these approximations n , α , and β can be rewritten as

$$\begin{aligned} n &\approx \sqrt{1 + \chi'} \approx 1 + \frac{1}{2}\chi' \\ \alpha &\approx -\frac{k_0}{n}\chi'' \\ \beta &\approx \left(1 + \frac{\chi'}{2}\right)k_0. \end{aligned} \quad (3.2)$$

In measurements, light from a well-known source is analysed after its interaction with

the vapour. The absorptive characteristics are described by the imaginary part of the susceptibility and are measured, directly. To retrieve the dispersive characteristics of the real part of χ from the transmission spectrum, the Kramers-Kronig relations can be employed as

$$\begin{aligned}\chi'(\nu) &= \frac{P}{\pi} \int_{-\infty}^{\infty} \frac{\chi''(s)}{s - \nu} ds \\ \chi''(\nu) &= \frac{P}{\pi} \int_{-\infty}^{\infty} \frac{\chi'(s)}{s - \nu} ds.\end{aligned}\tag{3.3}$$

Hereby, P is the Cauchy principal value.

3.2.2 Two-level system

This section treats a two-state atomic system coupled to a classical light field as depicted by figure 3.2. The basic concepts are outlined analogous to [Blo03] and [Bet16].

Pure states

The level scheme consists of a ground state $|g\rangle$ with energy $E_g = \hbar\omega_g$ and an excited state $|e\rangle$ with energy $E_e = \hbar\omega_e$. Hereby, \hbar is the reduced Planck constant and ω_k the angular frequency of the energy level $|k\rangle$. The frequency difference between the ground and excited state is defined as $\omega_{eg} = \omega_e - \omega_g$. The system interacts with monochromatic light with frequency ω_L .

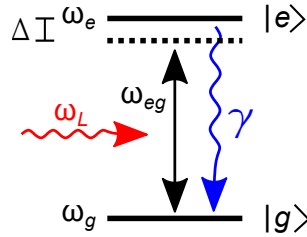


Figure 3.2: Schematics of a two-level atomic system consisting of the ground state $|g\rangle$ and an excited state $|e\rangle$.

The bare energies of the system are described by the Hamiltonian

$$\hat{H}_0 = E_g |g\rangle \langle g| + E_e |e\rangle \langle e|.\tag{3.4}$$

By setting $E_g = 0$ the equation simplifies to

$$\hat{H}_0 = \hbar\omega_{eg} |e\rangle \langle e|.\tag{3.5}$$

In the vector notation, the ground and excited state can be written as

$$|g\rangle = \begin{pmatrix} 1 \\ 0 \end{pmatrix} \quad \text{and} \quad |e\rangle = \begin{pmatrix} 0 \\ 1 \end{pmatrix}.\tag{3.6}$$

With this the free-atom Hamiltonian is

$$\hat{H}_0 = \begin{pmatrix} 0 & 0 \\ 0 & \hbar\omega_{eg} \end{pmatrix}. \quad (3.7)$$

The electric dipole operator is defined as

$$\hat{d} = \vec{d}_{eg} |e\rangle \langle g| + \vec{d}_{ge} |g\rangle \langle e| \quad (3.8)$$

with the dipole matrix element $\vec{d}_{eg} = \langle g | \vec{d} | e \rangle = -q \langle g | \vec{r} | e \rangle = \vec{d}_{eg}^*$. Here, q is the elementary charge and \vec{r} the position of the electron from its nuclei. The dipole matrix element of a transition is a measure of the interaction strength.

The interacting electric field $\vec{E}(\vec{r}, t)$, is described by a monochromatic plane wave.

$$\vec{E}(\vec{r}, t) = \frac{1}{2} (\vec{E}_0(\vec{r}) e^{-i\omega_L t} + \vec{E}_0^*(\vec{r}) e^{i\omega_L t}) \quad (3.9)$$

The atom-light field coupling is characterized by the interaction Hamiltonian

$$\hat{H}_{int} = -\hat{d} \cdot \vec{E}(\vec{r}, t). \quad (3.10)$$

for an atom at position \vec{r} . In the interaction picture the atom-light field coupling is represented by the following time dependent Schrödinger equation

$$i\hbar \frac{\partial}{\partial t} |\Psi(\vec{r}, t)\rangle = \hat{H} |\Psi(\vec{r}, t)\rangle \quad (3.11)$$

with $\hat{H} = \hat{H}_0 + \hat{H}_{int}$. It describes the time evolution of the quantum state $|\Psi(\vec{r}, t)\rangle$. We choose the general wave equation as an ansatz.

$$|\Psi(\vec{r}, t)\rangle = c_g(t) e^{-i\omega_g t} \cdot \hat{u}_g(\vec{r}) + c_e(t) e^{-i\omega_e t} \cdot \hat{u}_e(\vec{r}) \quad (3.12)$$

$e^{-i\omega_g t} \cdot \hat{u}_g(\vec{r})$ and $e^{-i\omega_e t} \cdot \hat{u}_e(\vec{r})$ are the eigenstates of \hat{H}_0 and describe the spatial distribution of the ground and excited state. By inserting equations 3.12 into equation 3.11 and applying a scalar product with $e^{-i\omega_j t} \cdot \hat{u}_j(\vec{r})$ we find

$$\begin{aligned} \frac{\partial}{\partial t} c_g(t) &= i \frac{\Omega_0}{2} (e^{i(\omega_L - \omega_{eg})t} + e^{-i(\omega_L + \omega_{eg})t}) c_e(t) \\ \frac{\partial}{\partial t} c_e(t) &= i \frac{\Omega_0}{2} (e^{-i(\omega_L - \omega_{eg})t} + e^{i(\omega_L + \omega_{eg})t}) c_g(t) \end{aligned} \quad (3.13)$$

where $\Omega_0 = \frac{d_{eg} E_0}{\hbar}$ is the Rabi frequency.

The rotating wave approximation states that terms in the Hamiltonian which oscillate rapidly can be neglected. For a close-to-resonance excitation, i.e. $\omega_L \approx \omega_{eg}$, the rapidly

oscillating $\omega_L + \omega_{eg}$ can be ignored. With $\Delta = \omega_L - \omega_{eg}$ equations 3.13 are simplified to

$$\begin{aligned}\frac{\partial}{\partial t}c_g(t) &= i\frac{\Omega_0}{2}e^{i\Delta t} \cdot c_g(t) \\ \frac{\partial}{\partial t}c_e(t) &= i\frac{\Omega_0}{2}e^{-i\Delta t} \cdot c_e(t).\end{aligned}\tag{3.14}$$

With $\tilde{c}_g(t) = c_g(t)e^{-i\Delta t/2}$ and $\tilde{c}_e(t) = c_e(t)e^{i\Delta t/2}$ we find the final differential system of equations

$$\frac{\partial}{\partial t} \begin{pmatrix} \tilde{c}_g(t) \\ \tilde{c}_e(t) \end{pmatrix} = \frac{i}{2} \begin{pmatrix} -\Delta & \Omega_0 \\ \Omega_0 & \Delta \end{pmatrix} \begin{pmatrix} \tilde{c}_g(t) \\ \tilde{c}_e(t) \end{pmatrix}\tag{3.15}$$

For a resonant excitation with $\Delta = 0$ and the initial condition of the whole population being in the ground state at $t = 0$, i.e. $\tilde{c}_g(0) = 1$ and $\tilde{c}_e(0) = 0$, the differential system of equations 3.15 leads to $\tilde{c}_g(t) = \cos\left(\frac{\Omega_0 t}{2}\right)$ and $\tilde{c}_e(t) = i \sin\left(\frac{\Omega_0 t}{2}\right)$. The population of the states is defined as the square of the absolute value.

$$\begin{aligned}|\tilde{c}_g(t)|^2 &= \cos^2\left(\frac{\Omega_0 t}{2}\right) \\ |\tilde{c}_e(t)|^2 &= \sin^2\left(\frac{\Omega_0 t}{2}\right)\end{aligned}\tag{3.16}$$

We see that population in the atomic system oscillates between ground and excited state with the Rabi frequency.

Including the detunings δ yields the general Rabi frequency $\Omega = \sqrt{\Delta^2 + \Omega_0^2}$, and the population in the excited state given by

$$|\tilde{c}_e(t)|^2 = \frac{\Omega_0^2}{\Omega^2} \sin^2\left(\frac{\Omega t}{2}\right).\tag{3.17}$$

Mixed states

Since the Schrödinger equation does not allow for decoherence, it has to be treated with the density matrix formalism. The density matrix ρ is defined as

$$\rho = \begin{pmatrix} \rho_{gg} & \rho_{ge} \\ \rho_{eg} & \rho_{ee} \end{pmatrix}\tag{3.18}$$

For pure states the following applies.

$$\rho = \begin{pmatrix} c_g c_g^* & c_g c_e^* \\ c_e c_g^* & c_e c_e^* \end{pmatrix}\tag{3.19}$$

In the density matrix representation, the diagonal elements are the populations, and the non-diagonal elements are the coherences of the atom-light coupling. With Liouville's

theorem

$$i\hbar \frac{\partial}{\partial t} \hat{\rho} = [\hat{H}, \hat{\rho}] \quad (3.20)$$

and equation 3.13 the density matrix elements can be calculated. To simplify the expression, a reference frame with frequency ω_L is chosen. The Lindblad operator \hat{L}

$$\hat{L} = \begin{pmatrix} \gamma\rho_{ee} & -\frac{1}{2}\gamma\rho_{ge} \\ -\frac{1}{2}\gamma\rho_{eg} & -\gamma\rho_{ee} \end{pmatrix} \quad (3.21)$$

is introduced to include spontaneous decay rates and other decoherence mechanisms which are not described by a unitary transform in γ . γ dampens the Rabi oscillations. With this, equation 3.20 transforms into the Lindblad master equation

$$i\hbar \frac{\partial}{\partial t} \hat{\rho} = [\hat{H}, \hat{\rho}] + i\hbar \hat{L}. \quad (3.22)$$

With γ , $\tilde{\rho}_{eg} = e^{-i\Delta t} \rho_{eg}$ and $\tilde{\rho}_{ge} = e^{-i\Delta t} \rho_{ge}$ the following so-called optical Bloch equations are derived.

$$\begin{aligned} \dot{\rho}_{gg} &= i\frac{\Omega_0}{2}(\tilde{\rho}_{ge} - \tilde{\rho}_{eg}) + \gamma\rho_{ee} \\ \dot{\rho}_{ee} &= -i\frac{\Omega_0}{2}(\tilde{\rho}_{ge} - \tilde{\rho}_{eg}) - \gamma\rho_{ee} \\ \dot{\rho}_{ge} &= -i\frac{\Omega_0}{2}(\rho_{ee} - \rho_{gg}) - \left(\frac{\gamma}{2} + i\Delta\right)\tilde{\rho}_{ge} \\ \dot{\rho}_{eg} &= i\frac{\Omega_0}{2}(\rho_{ee} - \rho_{gg}) - \left(\frac{\gamma}{2} - i\Delta\right)\tilde{\rho}_{eg} \end{aligned} \quad (3.23)$$

The total population is preserved through the condition $\rho_{gg} + \rho_{ee} = 1$. Furthermore, $\rho_{ge} = \rho_{ge}^*$ applies and γ , the natural decay rate, is defined as

$$\gamma = \frac{d_{eg}\omega_{eg}^3}{3\pi\epsilon_0\hbar c^3}. \quad (3.24)$$

Here, c is the speed of light, \hbar the reduced Planck constant, and ϵ_0 the vacuum permittivity. In the steady state, $\frac{\partial}{\partial t}\tilde{\rho}_{eg} = 0$ and $\frac{\partial}{\partial t}(\rho_{ee} - \rho_{gg}) = 0$. We find that $\rho_{ee} - \rho_{gg} = -\frac{1}{1+s}$ with the saturation parameter s

$$s = \frac{\Omega_0^2/2}{\Delta^2 + \gamma^2/4} = \frac{s_0}{1 + 4\Delta^2/\gamma^2}. \quad (3.25)$$

s_0 is the saturation parameter for the resonant system at $\delta = 0$. Furthermore, s_0 is defined as the relation between the intensity of the incoming light $I = \frac{1}{2}c\epsilon_0 E_0^2$ and the saturation intensity I_{sat} . With the lifetime of the excited state $\tau = 1/\gamma$ and the transition wavelength λ , this gives us the expression for the saturation intensity

$$I_{sat} = \frac{\pi\hbar c}{3\lambda^3\tau}. \quad (3.26)$$

3.2.3 Three-level system

The two-level system is expanded by a third level in this section. There are three types of three-level systems: the ladder, Λ , and V system. In this thesis only the Λ system is considered as depicted in figure 3.3. The derivation of the optical Bloch equations is analogous to the derivation of the two-level system and is summarized in this chapter similar to the treatment in [Eri12]. More details can be found in [FIM05].

The system is driven by a coupling and a probe laser, denoted by the index c and p, respectively.

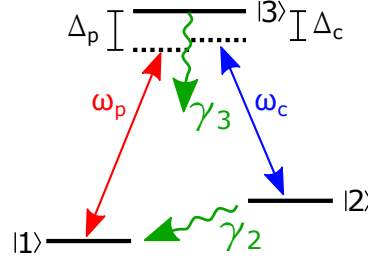


Figure 3.3: Schematic of a three-level scheme consisting of two ground states $|1\rangle$ and $|2\rangle$, and an excited state $|3\rangle$. The red arrow denotes the probe field ω_p . The blue arrow indicates the coupling light fields. The decays are depicted in green.

The interaction Hamiltonian for the three-level system includes the interaction energy of the additional third state. It can be rewritten as

$$\hat{H}_{int} = -\frac{\hbar}{2} \begin{pmatrix} 0 & 0 & \Omega_p \\ 0 & 2(\Delta_p - \Delta_c) & \Omega_c \\ \Omega_p & \Omega_c & 2\Delta_p \end{pmatrix} \quad (3.27)$$

with the rotating-wave approximation in a co-rotating frame with $\Delta_p = \omega_{31} - \omega_p$ and $\Delta_c = \omega_{32} - \omega_c$. ω_{31} and ω_{32} are the resonant transition frequencies between states $|3\rangle$ and the two ground states, $|1\rangle$ and $|2\rangle$.

The three-dimensional density matrix is

$$\rho = \begin{pmatrix} \rho_{11} & \rho_{12} & \rho_{13} \\ \rho_{12} & \rho_{22} & \rho_{32} \\ \rho_{13} & \rho_{23} & \rho_{33} \end{pmatrix}. \quad (3.28)$$

The Lindblad master equation defined in equation 3.22 can be rewritten as

$$\dot{\rho}_{ij} = -\frac{i}{\hbar} \sum_k (H_{ik} \rho_{kj} - \rho_{ik} H_{kj}) + \frac{1}{2} (\gamma_{ik} \rho_{kj} + \rho_{ik} \gamma_{kj}) \quad (3.29)$$

in component form. Solving it yields the diagonal elements

$$\begin{aligned}
 \dot{\rho}_{11} &= \frac{i\Omega_p}{2}(\rho_{21} - \rho_{12}) + \gamma_2\rho_{22} + \gamma_3\rho_{33} \\
 \dot{\rho}_{22} &= -\frac{i\Omega_p}{2}(\rho_{21} - \rho_{12}) - \gamma_2\rho_{22} \\
 \dot{\rho}_{33} &= \frac{i\Omega_c}{2}(\rho_{23} - \rho_{32}) - \gamma_3\rho_{33}
 \end{aligned} \tag{3.30}$$

with the total decay from state $|2\rangle$ γ_2 and the total decay from state $|3\rangle$ γ_3 . The off-diagonal elements are given by

$$\begin{aligned}
 \dot{\tilde{\rho}}_{12} &= -\frac{i\Omega_c}{2}\tilde{\rho}_{13} + \frac{i\Omega_p}{2}\tilde{\rho}_{32} - (\gamma_{21} - i(\Delta_c - \Delta_p))\tilde{\rho}_{12} \\
 \dot{\tilde{\rho}}_{13} &= \frac{i\Omega_p}{2}(\tilde{\rho}_{33} - \tilde{\rho}_{11}) - \frac{i\Omega_c}{2}\tilde{\rho}_{12} - (\gamma_{31} + i\Delta_p)\tilde{\rho}_{13} \\
 \dot{\tilde{\rho}}_{23} &= \frac{i\Omega_c}{2}(\tilde{\rho}_{33} - \tilde{\rho}_{22}) - \frac{i\Omega_p}{2}\tilde{\rho}_{21} - (\gamma_{32} + i\Delta_c)\tilde{\rho}_{23}
 \end{aligned} \tag{3.31}$$

with $\gamma_{ij} = \frac{1}{2}(\gamma_i + \gamma_j)$. The total population is constant and thus state $|1\rangle$ does not decay. In steady state $\dot{\tilde{\rho}}_{12} = \dot{\tilde{\rho}}_{13} = \dot{\tilde{\rho}}_{23} = 0$.

Electromagnetically induced transparency - EIT

The strong coupling laser depopulates states $|2\rangle$ and $|3\rangle$ the population is trapped in the non-emitting dark state $|1\rangle$, i.e. $\tilde{\rho}_{11} \approx 1$ and $\tilde{\rho}_{22} \approx \tilde{\rho}_{33} \approx 0$. This effect is called electromagnetically induced transparency [FIM05] - short EIT. With the assumption of a strong coupling light field the equations of motion can be simplified to

$$\begin{aligned}
 \dot{\tilde{\rho}}_{12} &= -\frac{i\Omega_c}{2}\tilde{\rho}_{13} - (\gamma_{21} - i(\Delta_c - \Delta_p))\tilde{\rho}_{12} \\
 \dot{\tilde{\rho}}_{13} &= -\frac{i\Omega_p}{2}\tilde{\rho}_{12} - \frac{i\Omega_c}{2}\tilde{\rho}_{12} - (\gamma_{31} + i\Delta_p)\tilde{\rho}_{13} \\
 \dot{\tilde{\rho}}_{23} &= -\frac{i\Omega_p}{2}\tilde{\rho}_{21} - (\gamma_{32} + i\Delta_c)\tilde{\rho}_{23}.
 \end{aligned} \tag{3.32}$$

The first two terms are a coupled pair of equations. They are solved as

$$\begin{aligned}
 \tilde{\rho}_{12} &= \frac{\Omega_c\Omega_p}{4(i\gamma_{21} + \Delta_c - \Delta_p)(-i\gamma_{31} + \Delta_p) + \Omega_c^2} \\
 \tilde{\rho}_{13} &= -\frac{2(\gamma_{21} - i(\Delta_c - \Delta_p))\Omega_p}{4(\gamma_{31} + i\Delta_p)(-i\gamma_{21} - \Delta_c + \Delta_p) - i\Omega_c^2}.
 \end{aligned} \tag{3.33}$$

The polarization \vec{P} is defined as

$$\vec{P} = \varepsilon_0\chi\vec{E} = NTr(\rho\vec{d}) \tag{3.34}$$

where ε_0 is the vacuum permittivity, χ the susceptibility introduced in section 3.2.1, \vec{E} the electric light field, N the number of atoms per volume, and \vec{d} the transition dipole moment introduced in the two-level system. Solving the equation for χ as described in [Eri12] yields

$$\chi = \frac{2N|\vec{d}_{13}|}{E_{0,p}\varepsilon_0} \tilde{\rho}_{13}. \quad (3.35)$$

Including $\tilde{\rho}_{13}$ from equation 3.33 and separating χ into real χ' and imaginary χ'' parts gives us

$$\begin{aligned} \chi' &= -\frac{2N|\vec{d}_{13}|\Omega_p}{E_{0,p}\varepsilon_0} \frac{2(4(\gamma_{21}^2 + (\Delta_c - \Delta_p)^2)\Delta_c + (\Delta_c - \Delta_p)\Omega_p^2)}{16(\gamma_{21}^2 + (\Delta_c - \Delta_p)^2)(\gamma_{31}^2 + \Delta_p^2) + 8(\gamma_{21}\gamma_{31} + (\Delta_c - \Delta_p)\Delta_p)\Omega_c^2 + \Omega_c^4} \\ \chi'' &= \frac{2N|\vec{d}_{13}|\Omega_p}{E_{0,p}\varepsilon_0} \frac{2(4\gamma_{31}(\gamma_{21}^2 + (\Delta_c - \Delta_p)^2) + \gamma_{21}\Omega_c^2)}{16(\gamma_{21}^2 + (\Delta_c - \Delta_p)^2)(\gamma_{31}^2 + \Delta_p^2) + 8(\gamma_{21}\gamma_{31} + (\Delta_c - \Delta_p)\Delta_p)\Omega_c^2 + \Omega_c^4} \end{aligned} \quad (3.36)$$

The absorptive behaviour of the light passing through the vapour is included in χ'' , and the refractive properties are described with χ' . Without the coupling laser, i.e. $\Omega_c = 0$, the system transforms into a two-level system and equations 3.36 simplify to

$$\begin{aligned} \chi' &= -\frac{2N|\vec{d}_{13}|\Omega_p}{E_{0,p}\varepsilon_0} \frac{\Delta_p}{\Delta_p^2 + \gamma_{31}^2} \\ \chi'' &= -\frac{2N|\vec{d}_{13}|\Omega_p}{E_{0,p}\varepsilon_0} \frac{\gamma_{31}}{\Delta_p^2 + \gamma_{31}^2}. \end{aligned} \quad (3.37)$$

Figure 3.4 shows the susceptibility plots with $\gamma_{21} = 0$. In a) the coupling laser is turned off and a Lorentzian absorption profile as predicted by equation 3.37 is obtained. Figure 3.4 b) shows an EIT feature with $\Omega_c = 0.5/\gamma_{31}$ with on-resonant transparency at a zero probe detuning. This induced transparency width is called transparency window. For high coupling intensities the EIT window develops into Autler-Townes doublets.

The width of the transparency window $\Delta\omega_{\text{trans}}$ for resonance of $\Delta_p - \Delta_c = 0$ is given by [FIM05]

$$\Delta\omega_{\text{trans}} = \frac{\Omega_c^2}{\sqrt{(\Gamma_1 + \Gamma_2)(\Gamma_1 + \Gamma_2 + \gamma_{3\text{deph}})}} \frac{1}{\sqrt{n_d\sigma z}}. \quad (3.38)$$

Here, $n_d\sigma z$ is the optical density of the medium as discussed in chapter 3.4.1 and $\gamma_{3\text{deph}}$ the dephasing rate of the ground states. As can be inferred for large bandwidths, high Rabi frequencies and low optical densities are required.

Figure 3.5 shows the transparency window dependent on counter- or co-propagating probe and coupling light fields. Plots a) and b) show the velocity classes addressed by the beams. c) and d) display the sum over all of the velocity classes. Counter-propagating light fields have an EIT feature at $\Delta_p = 0$. In a co-propagating scheme the sum over all velocity classes yields to no feature.

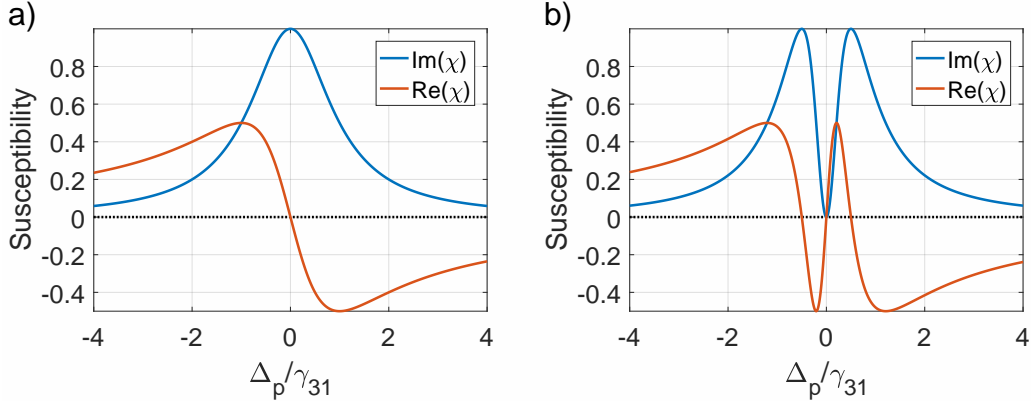


Figure 3.4: Real and imaginary parts of the susceptibility in a three-level system. The real part describes the absorption, the imaginary part describes the dispersive behaviour. In a) the line shapes are shown without the coupling laser. In b) the coupling Rabi frequency Ω_c equals $0.5/\gamma_{31}$. There is no decay between states $|1\rangle$ and $|2\rangle$.

Figure 3.6 a) shows the behaviour of the transparency window as a function of the probe and coupling detuning. At two-photon resonance $\Delta_c - \Delta_p = 0$, the feature is the deepest. Detuning the lasers from this resonance results in an asymmetric splitting of χ'' . The behaviour with respect to the coupling power is shown in b). By increasing the coupling Rabi frequency the depth and the overall splitting of the feature increases. For the regime with very high Ω_c , EIT doublets are called Autler-Townes doublets.

Slow light

The group velocity v_{gr} of a wave is the velocity with which the envelope of a wave propagates. It is defined as

$$v_{\text{gr}} = \frac{c}{n(\omega) + \omega \frac{\partial n}{\partial \omega}} = \frac{c}{n_{\text{gr}}}. \quad (3.39)$$

The dispersion of the group index n_{gr} is dependent on the susceptibility of the medium and is defined by the gradient of χ'' . Therefore, in an EIT scheme n_{gr} can be manipulated with the coupling power.

Figure 3.7 shows the behaviour of the imaginary part of the susceptibility, the corresponding refractive index n and the group index n_{gr} for an EIT feature with $\Omega_c = 10\Omega_p$. The simulation is done with a cell temperature of 20°C and a cell length L of 7.5 cm for the $6^2\text{S}_{1/2}$ to $6^2\text{P}_{1/2}$ transition in caesium. $E_{0,p}$ is set to 1 N/C . The group index is proportional to the derivation of the refractive index in respect to the frequency. A steep slope of n at $\Delta_p = 0$ leads to an increased group index. The increased group index

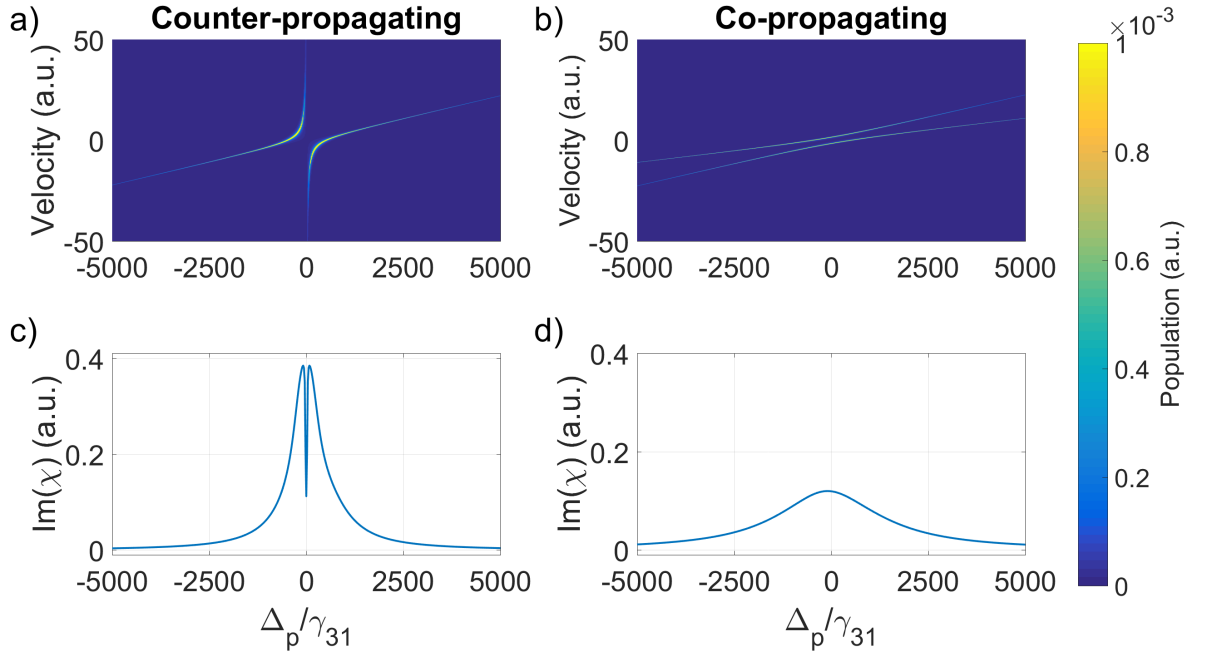


Figure 3.5: The EIT feature dependency on counter or co-propagating probe and coupling light fields. In a) and b) the velocity classes as a function of the probe detuning are plotted. The colour bar visualizes the value of the population. In c) and d) the population is summed up over all velocity classes leading to the familiar EIT feature for the counter-propagating case. In a co-propagating scheme the feature vanishes.

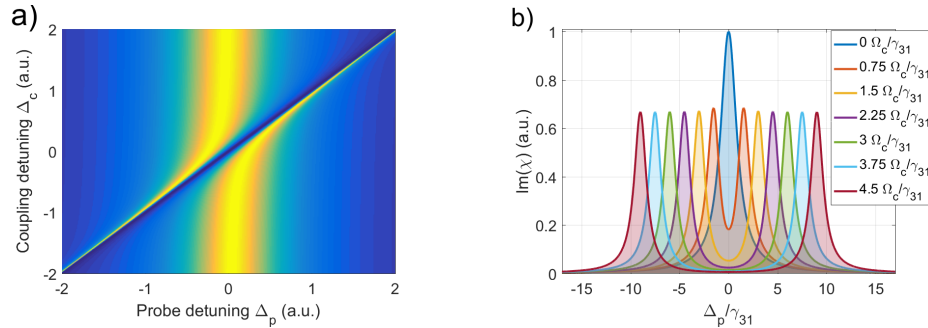


Figure 3.6: a) EIT feature versus probe and coupling laser detuning. Lighter colors refer to higher values of χ'' . b) χ'' for different coupling powers.

corresponds to a group delay τ_{gr} given by

$$\tau_{\text{gr}} = L \left(\frac{1}{v_{\text{gr}}} - \frac{1}{c} \right) = \frac{L}{c} n_{\text{gr}}. \quad (3.40)$$

This allows the propagating probe light to be controllably delayed. With this scheme the speed of light was reduced to 17 m/s in the year 1999 [HHDB99]. The group index for

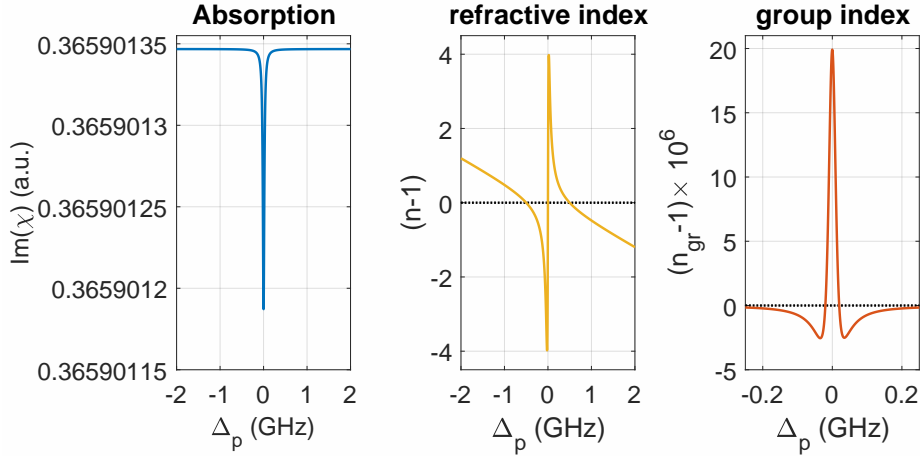


Figure 3.7: The imaginary part of the susceptibility of an EIT feature with $\Omega_c = 10\Omega_p$, $\gamma_{21} = 0.02$ Hz, γ_{31} the natural decay rate of the $6^2S_{1/2}$ to $6^2P_{1/2}$ transition in caesium and its corresponding refractive index n and group index n_{gr} .

various coupling powers is shown in figure 3.8. At a probe detuning $\Delta_p = 0$ the group index has the highest values. This slowdown can be used as a basis for light storage. The basic principle of this storage scheme is discussed in the following section.

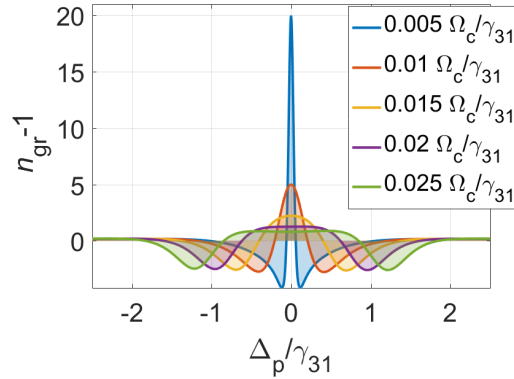


Figure 3.8: Group index n_{gr} for various coupling Rabi frequencies. With decreasing Rabi frequency the group index at resonance increases.

3.3 Basic principle of the EIT storage scheme

As described in section 3.2.3, it is possible to manipulate the transparency of a medium with a coupling field in an EIT scheme [FIM05]. By turning off the coupling light and substantially increasing the absorption of the system, formerly propagating light can be “stopped”. Herefore, a mathematical frame describing slow light and storage processes similar to [Ott11] is introduced. It proves that storage schemes in contrast to slow light

schemes need temporally varying light fields. Furthermore, the timing of the laser fields are discussed.

Atomic transitions can be expressed as $\hat{\sigma}_{ij} = |i\rangle \langle j|$. For simplicity these operators are reduced to the slowly varying operators

$$\begin{aligned}\hat{\sigma}_{13} &= \hat{\tilde{\sigma}}_{13} e^{-i\omega_p t + ik_p z} \\ \hat{\sigma}_{23} &= \hat{\tilde{\sigma}}_{23} e^{-i\omega_c t + ik_c z}\end{aligned}\quad (3.41)$$

similar to the rotating wave approximation. Parallel to the derivation of the density matrix elements a set of equations fulfilling the Lindblad master equation can be found for these projection operators. They can be written as

$$\left(\frac{\partial}{\partial t} + c \frac{\partial}{\partial z} - i \frac{c}{2k_p} \nabla_{\perp}^2 \right) \hat{\mathcal{E}}(\vec{r}, t) = i g n_d \hat{\sigma}(\vec{r}, t)_{13}. \quad (3.42)$$

In the above equation, $\hat{\mathcal{E}}(\vec{r}, t)$ is the slowly varying envelope of the electric field operator. g is the coupling strength of the probe field defined as $\frac{d_{13}}{h} \sqrt{\frac{\hbar \omega_p}{2\varepsilon_0}}$. n_d is the atomic density. In a medium with linear response and a weak probe beam compared to the coupling beam, the Bloch equations can be expressed as

$$\left(\frac{\partial}{\partial t} + c \frac{\partial}{\partial z} \right) \hat{\mathcal{E}} = i g n_d \hat{\sigma}_{13}^{(1)} \quad (3.43)$$

in first order perturbation theory with a neglected γ_{21} . Assuming that the coherence of the excited state is changing slowly in time and $\frac{\partial}{\partial t} \hat{\sigma}_{13} \approx 0$ we have

$$\begin{aligned}\left(\frac{\partial}{\partial t} + c \frac{\partial}{\partial z} \right) \hat{\mathcal{E}} &= -\frac{g^2 n_d}{\Gamma} \hat{\mathcal{E}} - \frac{g n_d \Omega_0}{\Gamma} \hat{\sigma}_{12} \\ \frac{\partial}{\partial t} \hat{\sigma}_{12} &= -i \Delta \hat{\sigma}_{12} - \frac{|\Omega|^2}{\Gamma} \hat{\sigma}_{12} - \frac{g n_d \Omega_0}{\Gamma} \hat{\mathcal{E}}\end{aligned}\quad (3.44)$$

with $\Gamma = \gamma_{31} + i\Delta$ and $\Delta = \Delta_p - \Delta_c$. By further assuming $|\Gamma \Delta| \ll |\Omega_0|^2$ and defining the mixing angle ϑ through

$$\tan^2(\vartheta) = \frac{g^2 n_d}{|\Omega_c|^2} \quad (3.45)$$

we find

$$\left(\frac{\partial}{\partial t} + c \cos^2(\vartheta) \frac{\partial}{\partial z} \right) \hat{\mathcal{E}} = -\Delta \left(i + \frac{\Gamma \Delta}{|\Omega_0|^2} \right) \sin^2(\vartheta) \hat{\mathcal{E}}. \quad (3.46)$$

For $\Delta \approx 0$ this wave equation is solved by a wave with the envelope $\hat{\mathcal{E}}(\vec{r}, t)$ and group velocity v_{gr}

$$v_{\text{gr}} = c \cdot \cos^2(\vartheta). \quad (3.47)$$

For $\vartheta \rightarrow 0$ the group velocity is approximately the speed of light. In the limit of $\vartheta \rightarrow \pi/2$

the group velocity approaches 0 and is mainly made up of a spin coherence excitation of states $|1\rangle$ and $|2\rangle$. ϑ can be varied by the coupling Rabi frequency Ω_c as described by equation 3.45.

If light is stopped, i.e. $v_{\text{gr}} \rightarrow 0$, the dispersion of the susceptibility has to asymptotically approach infinity as shown in figure 3.7 b). This requires an infinitesimal narrow transparency window. In practice this is not possible without a time-dependent coupling field which induces a time dependence of ϑ .

The time dependent EIT scheme can be separated into three time sequences as shown by figure 3.9.

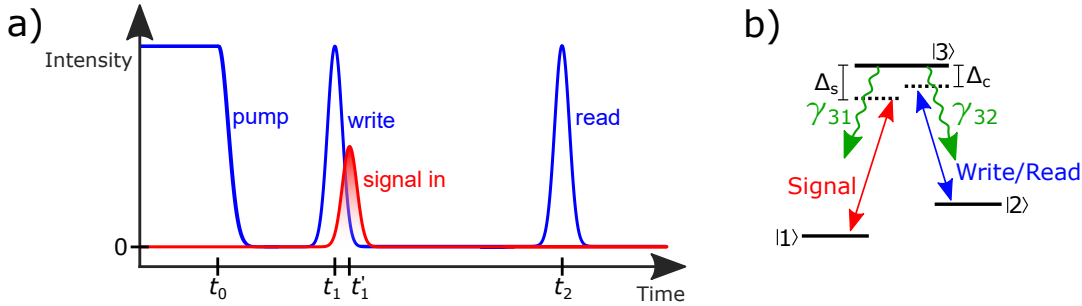


Figure 3.9: a) Laser sequences of the storage process and b) its corresponding lambda level scheme. The indices s and c refer to the signal and coupling fields, respectively. The times t_1 and t'_1 denote the time in which the write and signal fields are sent into the cell, respectively. They share the same value in a off resonant Raman scheme. In an on resonant stimulated Raman adiabatic passage (STIRAP) scheme t'_1 is slightly delayed as depicted in a).

t_0 : By optically pumping with a strong continuous-wave laser resonant to the coupling beam transition, the population is prepared in state $|1\rangle$. Here, $|1\rangle$ can be treated as a dark state in which the whole population is trapped.

t_1 : In a Raman scheme the times t_1 and t'_1 share the same value [TMK⁺17] [WBH⁺17]. The signal to be stored and the strong write field are sent into the medium simultaneously. Hereby, the Raman scheme refers to an off-resonant scheme in which photons are scattered inelastically from an atom. In an on-resonant stimulated Raman adiabatic passage (STIRAP) scheme, t'_1 is slightly delayed such that write and signal fields still overlap as depicted in figure 3.9 a) [BVS15]. In both schemes the signal is mapped onto a collective spinwave excitation between the coherence of states $|1\rangle$ and $|2\rangle$.

t_2 : Through a read pulse the collective spinwave excitation is retransformed into a light field and the stored signal is read out. The read out signal shares the same quantum properties as the incident signal.

3.3.1 Limitations

The efficiency of storage processes is a measure for the probability with which a single photon can be read out after a storage procedure. It is defined as [Rei11]

$$\eta = \frac{N_{out}}{N_{in}} \quad (3.48)$$

with the number of read out photons being N_{out} and the number of incident photons N_{in} . The efficiency is mainly limited by the following disruptive processes.

Ground state decoherence

The storage time is mainly limited by the ground state decoherence γ_{21} . γ_{21} is the sum of the following processes [VGL98].

- **Collisional decay rate (γ_{col}):** By colliding with other caesium atoms the coherence of the ground state gets destroyed. For times between t_0 and t_1 the optical pumping efficiency is reduced by collisions, and after t_1 the storage time is limited by the destruction of the coherence of a stored signal limiting the storage time. The collisional decay rate can be approximated by

$$\gamma_{col} = n_d \sigma \bar{v} \quad (3.49)$$

for the mean velocity $\bar{v} = \sqrt{\frac{8k_B T}{\pi m}}$, the Boltzmann constant k_B , the temperature T , and the mass of one caesium atom m .

- **Spin exchange collisions (γ_{SE}):** In contrast to the collisional decay rate, γ_{SE} only includes collisions changing the spin of the ground states. Hereby, the spin of the colliding atoms is preserved. The decay is given by

$$\gamma_{SE} = n_d \sigma_{SE} \bar{v} \cdot R. \quad (3.50)$$

In this equation R is defined as

$$R = \frac{6I + 1}{8I + 4} = 0.687 \quad (3.51)$$

with the nuclear spin $I = 7/2$. R defines the basic ratio of the coherence spin exchange relaxation rate and the collisional decay rate. It can be found by analysing the manifold of the hyperfine levels and assuming a perfectly pumped system.

- **Caesium-buffer gas collisions (γ_{cs-buf}):** In the presence of a buffer gas collisions with the buffer gas can destroy the ground state coherence. The decay rate is given by

$$\gamma_{cs-buf} = n_O \cdot \bar{v}_{mixture} \cdot \sigma_{cs-buf}. \quad (3.52)$$

Here, n_O is the Loschmidt constant and $\bar{v}_{\text{mixture}} = \sqrt{\frac{8k_B T}{\pi\mu}}$ with the reduced mass μ .

- **Collisions with walls and diffusion (γ_{walls}):** The collisions with walls for a cylindrical cell are summarized in

$$\gamma_{\text{walls}} = \left(\left(\frac{2.405}{z_d} \right)^2 + \left(\frac{\pi}{L} \right)^2 \right) \cdot D \quad (3.53)$$

where D is the diffusion constant, z_d the cell diameter, and L the cell length. In general, it is sufficient to only take into account the first mode of diffusion. This assumption is included in the value 2.405 which is the first root of the Bessel function. This decay can be suppressed by applying a coherence preserving paraffin coating to the cell walls [TMK⁺17] and using cells with a large diameter and length.

Atoms carrying the stored signal can diffuse out of the interaction volume set by the spatial proportions of the laser beams. They are replaced by atoms diffusing into the beams. This exchange of prepared atoms with unprepared atoms can be treated as a collision with the wall with a diameter z_d being the diameter of the signal beam [SNH96].

Bandwidth and optical density

Additionally, the bandwidth of the signal $\Delta\omega_s$ is limited by the bandwidth of the EIT transparency window $\Delta\omega_{\text{trans}}$ defined in section 3.2.3 by equation 3.38. To keep the whole photon $\Delta\omega_s \ll \Delta\omega_{\text{trans}}$ needs to apply. In terms of the group delay $\Delta\omega_{\text{trans}}$ can be expressed as

$$\Delta\omega_{\text{trans}} = \frac{\sqrt{n_d \sigma z}}{\tau_{\text{gr}}} \sqrt{\frac{\Gamma_1}{\Gamma_1 + \Gamma_2 + \gamma_{3\text{deph}}}}. \quad (3.54)$$

Considering the pulse length of the signal field τ_{pulse} and $\Delta\omega_{\text{pulse}} \tau_{\text{gr}} \geq 1$

$$\frac{\tau_{\text{gr}}}{\tau_{\text{pulse}}} \ll \sqrt{n_d \sigma z}. \quad (3.55)$$

$n_d \sigma z$ is the optical density of the medium. Therefore, for long delays high optical densities are needed. This furthermore reduces the risk of cutting off the pulse as a consequence of not fitting into the cell. This is the case if $\tau_{\text{pulse}} v_{\text{gr}} \ll L$. Figure 3.10 depicts the pulse deformation dependent on the group velocity v_{gr} introduced in equation 3.39 for a frequency independent refractive index. For $v_{\text{gr}} < c$ the pulse gets compressed, for $v_{\text{gr}} = c$ it does not get deformed, and for $v_{\text{gr}} > c$ it gets broadened.

Increased optical densities however, lead to higher absorption and a higher probability of collisions which destroy the coherence and collisions leading to the spin-flipping of

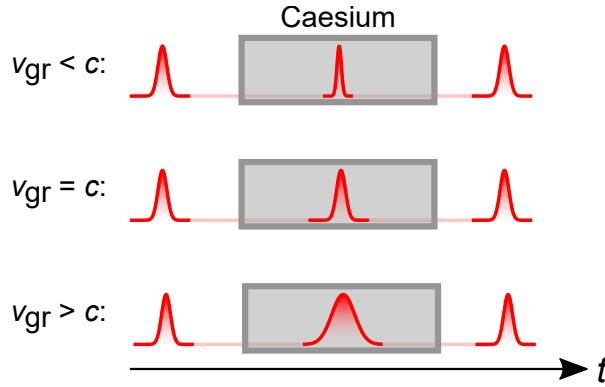


Figure 3.10: Scheme of the signal pulse compression and broadening through a caesium vapour cell dependent on the group velocity v_{gr} for a frequency independent refractive index.

the prepared atoms. Furthermore, radiation trapping is increased with increasing optical densities. Higher optical densities are feasible by including buffer gases. The optimal optical density is a trade-off between various processes.

Optical pumping and radiation trapping

The storage protocol needs atoms prepared in state $|1\rangle$ by optical pumping. Already prepared atoms drift out of the coupling laser beam and are replaced by unpumped atoms from the surrounding. Effectively, this leads to a lowered lifetime of the pumped system. This was already introduced in equation 3.53. The diffusion can be reduced by adding buffer gases [TMK⁺17] and choosing wider geometrical spatial modes of the pump laser.

Radiation trapping is a process in which resonant radiation is trapped in a vapour by multiple re-absorptions [TMK⁺17]. Through the optical pumping process in which population decays from state $|3\rangle$ into state $|1\rangle$, on-resonant radiation is generated in a large scale. The re-absorbed photons de-excite the excited atoms hence, reducing the overall efficiency of the pumping. Furthermore, radiation trapping creates an on-resonant radiation background which is challenging to filter in single photon storage protocols. The re-absorbing process increases exponentially with the number density. Buffer gases with vibrational transitions close to the caesium transition can absorb these trapped photons and reduce the disruptive background through the so-called collisional quenching.

Four-wave mixing background

The strong coupling light field creates an artificial state as shown by figure 3.11. This induces a slightly detuned Stokes field α which repopulates state $|2\rangle$ and undermines the optical pumping efficiency. In the write sequence at t_1 , population in $|2\rangle$ is excited to $|3\rangle$ and induces an on-resonant decay from $|3\rangle$ to $|1\rangle$. This four-wave mixing background is

impossible to be completely filtered out in single photon storage processes as it is exactly at the same frequency since the stored light field.

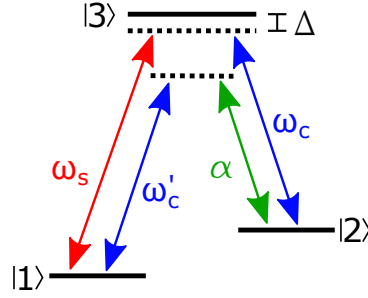


Figure 3.11: Four-wave mixing scheme. The strong signal field creates an artificial state through which the population is transferred from state $|1\rangle$ to state $|2\rangle$ by an additional Stokes transition denoted by α .

Magnetic field gradients

Magnetic field gradients cause dephasing which can be thought of as the destruction of the phase relationship of collective excitations. Through this process the collective excitation can not be addressed by laser fields and are considered as destroyed. Dephasing is characterised by the extinction of the decoherences of the collective spin-wave excitation and limits the storage time. By magnetic shielding through μ -metal the magnetic field from the earth is suppressed. μ -metal is an alloy characterized by a very high permeability.

3.4 Spectroscopy

Spectroscopy is a method exploring the interaction of light with matter. Light travels through a medium and is analysed afterwards. This method gives information concerning the medium and the nature of the interaction. More details can be looked up in [Dem11] and [Dem13]. This chapter highlights the principles used in this thesis.

3.4.1 Optical density

Light entering atomic vapours interacts with the medium. The Beer–Lambert law describes the absorption of light travelling through a vapour [Sid14]. It is generally expressed as

$$I(z) = I_0 e^{-\alpha z} = I_0 e^{ikz\chi/2}. \quad (3.56)$$

Here, I is the intensity after a distance z through the vapour cell. I_0 is the intensity of the probe before the cell, α is the attenuation coefficient introduced in equation 3.2, and χ is the electric susceptibility as described in section 3.2.1. Through evaluating the transmission spectrum and transforming the data with the Kramers-Kronig-relations it

is possible to retrieve the real and imaginary parts of the susceptibility. The intensity loss is accredited to the absorption of photons. The optical density OD is defined as

$$\text{OD} = \alpha z. \quad (3.57)$$

The attenuation coefficient α is

$$\alpha = \frac{\alpha_0}{1 + 4(\Delta/\gamma)^2} \quad (3.58)$$

with the detuning Δ , the decay rate γ , and the resonant absorption coefficient α_0 defined as

$$\alpha_0 = n_d \cdot \sigma_{ge} = n_d \cdot \frac{\hbar\omega_L\gamma}{2I_{\text{sat}}} = \frac{3\lambda^2}{2\pi}. \quad (3.59)$$

In this formular, n_d is the number density, σ_{ge} is the on-resonant cross section for the transition from $|g\rangle$ to $|e\rangle$, λ is the interaction wavelength, and I_{sat} is the saturation intensity as defined in equation 3.26. In the range of temperatures used in these experiments the ideal gas law applies. With the vapour pressure given in [Ste10] the atomic density \tilde{n} can be expressed as

$$\tilde{n}(T) = \frac{1.0133}{k_B T} \cdot e^{9.165 - \frac{3830}{T}} \quad (3.60)$$

where T is the temperature in Kelvin and k_B is the Boltzmann constant. Thus, by increasing the temperature of the vapour it is possible to increase the OD.

3.4.2 Broadening mechanisms

The frequency of emitted light is not strictly monochromatic, but has a frequency distribution around a central wavelength. Various broadening mechanisms increase the linewidth to values above the natural linewidth. The linewidth is synonymous with the decay rate of the specified tranistion. This section gives an overview of the broadening mechanisms as descibed in [Dem11]. The line profile is described by a Voigt profile V which mathematically consists of the convolution of a Gaussian $G(\omega)$ and a Lorentzian $L(\omega' - \omega)$ part and is described as

$$V = V_0 \int_{-\infty}^{\infty} G(\omega)L(\omega' - \omega)d\omega \quad (3.61)$$

with

$$G(\omega) = \frac{1}{\sigma\sqrt{2\pi}} e^{-\omega^2/(2\sigma^2)} \quad (3.62)$$

and

$$L(\omega' - \omega) = \frac{\gamma/2}{\pi((\omega' - \omega)^2 + (\gamma/2)^2)}. \quad (3.63)$$

The major mechanisms are presented in the following. The natural, pressure, and transit time broadening mechanisms are homogeneous broadening mechanisms and contribute

a Lorentzian profile. The remaining mechanisms are inhomogeneous providing the Gaussian shaped frequency distribution.

Natural broadening

The frequency distribution is naturally broadened as a consequence of the uncertainty principle relating the energy of an excited state E with its lifetime τ .

$$\Delta E \cdot \Delta \tau \geq \hbar \quad (3.64)$$

The uncertainty of the energy results in a broadened Lorentzian shaped profile. The linewidth τ_k of state $|k\rangle$ is defined by its Einstein coefficient A_k .

$$\tau_k = \frac{1}{A_k} \quad (3.65)$$

Doppler broadening

Doppler broadening mechanisms are dominant in vapours. It is caused by the Maxwellian distribution of the atom velocities due to a finite temperature. If an atom moves while emitting a photon, the Doppler effect shifts its natural frequency ω_0 to the frequency ω according to

$$\omega = \omega_0 + \vec{k}\vec{v} \quad (3.66)$$

where \vec{k} is the wavevector of the emitted photon and \vec{v} is the velocity of the atom. The resulting line profile is a Gaussian distribution with the width σ given by

$$\sigma = \frac{\omega_0}{c} \sqrt{\frac{8k_B T \cdot \ln(2)}{m}}. \quad (3.67)$$

The Doppler broadening is dominating the natural broadening by about 1-2 orders in magnitude.

Pressure broadening

Pressure broadening results from atom-atom collisions. Elastic collisions distort the energy levels of both atoms and cause shifts of the transition frequencies. Inelastic collisions, the so-called quenching collisions, transfer energy of an excited state to the other atom thus reducing the fluorescence of the originally excited state. Elastic and inelastic collisions lead to a Lorentzian distribution with

$$\gamma = \gamma_{elastic} + \gamma_{inelastic}. \quad (3.68)$$

Power broadening

The population of the excited state increases at higher laser intensities I . Very high intensities lead to an occupation number density that converges to 0.5 in steady state.

In this case, the absorption coefficient α converges to 0 and the vapour is transparent for light with the same wavelength. Induced emission and absorption balance each other. It contributes a Gaussian beam shape with line width σ

$$\sigma = \Delta\omega_0\sqrt{1 + s_0} \quad (3.69)$$

where s_0 is the saturation parameter defined in equation 3.26.

Transit time broadening

Transit time broadening is a consequence of the velocity v of the atoms. The probability of an atom moving with v is given by the Maxwell-Boltzmann function

$$f(v) = \left(\frac{m}{2\pi k_B T}\right)^{3/2} 4\pi v^2 e^{-mv^2/(2k_B T)} \quad (3.70)$$

and defines the probability of the velocity v of an atom and finite excitation volumes. The interaction of the atom with light is limited to the time it is located within the beam. The transit time is usually larger than the lifetime of excited states. For typical values such as a beam waist of $100\ \mu\text{m}$ and velocities of $300\ \text{m/s}$ a crossing atom would need $67\ \mu\text{s}$ which is significantly greater than the natural lifetime of excited states which is of the order of nanoseconds. For very small laser beam diameters however, the linewidth is narrowed by the transit time and not by the lifetime. Figuratively, on average a single excited atom leaving the beam is replaced by an atom in the ground state entering the beam. Assuming a Gaussian-shaped beam with diameter z_d is vertically crossed by an atom with the velocity \bar{v} , a Gaussian with linewidth σ describes the line profile [Dem11].

$$\sigma = \frac{4\bar{v}}{z_d} \sqrt{2\ln(2)}. \quad (3.71)$$

Hereby, \bar{v} is the root mean square of the total velocity and in three dimensions is

$$\bar{v} = \sqrt{\frac{3k_B T}{m}}. \quad (3.72)$$

4 Experimental setup

This chapter describes the experimental setup which was build as part of the thesis and used for the measurements in chapter 5 are done. This chapter gives an overview of the setup before treating the single components individually. Hereby, the emphasise lies on the reasons for choosing the components in respect to future quantum memory experiments. Further improvements to the setup needed to implement single-photon storage are discussed in chapter 6.

Figure 4.1 shows the schematic of the setup. Optical elements concerning the beam shaping were left out to simplify the sketch. The blue laser beam excites the coupling transition and is depicted in blue merely to differentiate signal and coupling fields. The following sections treat the single components in detail.

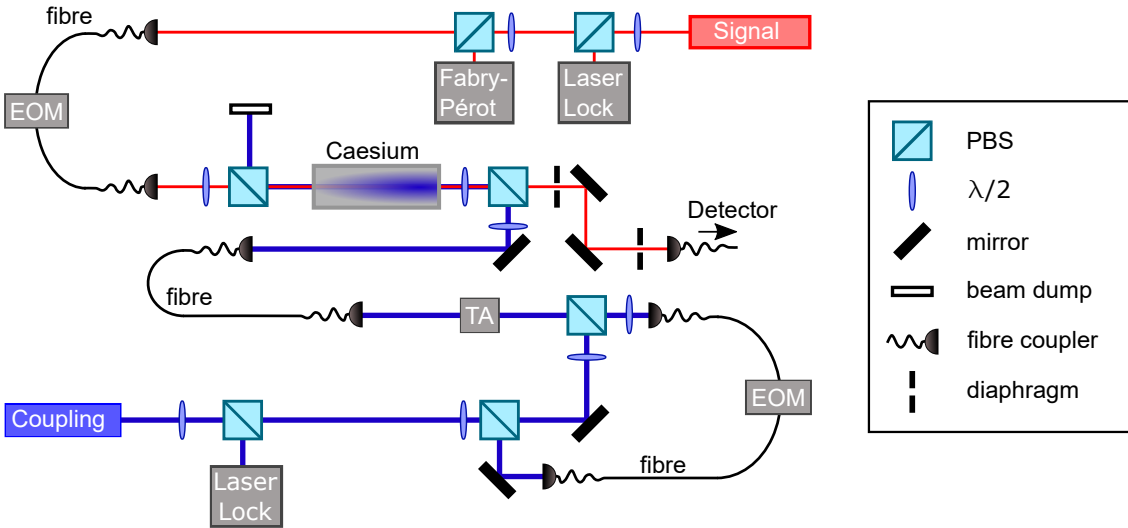


Figure 4.1: Schematics of the experimental setup. The blue colour of the laser beam was merely chosen to differentiate between coupling and signal beam. The fibres are polarisation maintaining fibres. Beam shaping optics are not included for better clarity.

4.1 Self-built diode laser

The signal field for the EIT measurements is generated with a self-built diode laser in a wavelength selective external cavity configuration. This so-called Littrow configuration is schematically represented in figure 4.2.

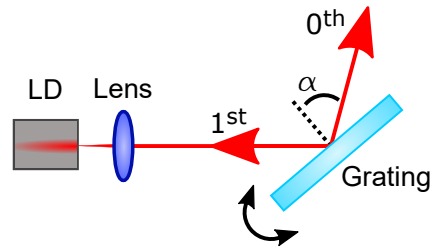


Figure 4.2: Schematic of the Littrow configuration. α denotes the diffraction angle. LD is the abbreviation of laser diode. The Littrow configuration stabilizes the laser diode, narrows its linewidth, and enables the tuning of the wavelength to a certain value.

In the Littrow configuration the first order diffracted beam is coupled back into the laser diode serving as an external cavity as depicted by figure 4.2. The 0th order is reflected and serves as the working beam. The configuration stabilizes the wavelength, narrows the linewidth of the laser to less than 1 MHz, and enables the tuning of the wavelength to a certain value. The fine tuning is done by the adjustment of the diffraction angle α and the applied voltage offset of the piezoelectric transducer. Laser diodes in this setup are called external-cavity diode lasers (ECDL). The setup is shown in figure 4.3. The single components are treated in the following.

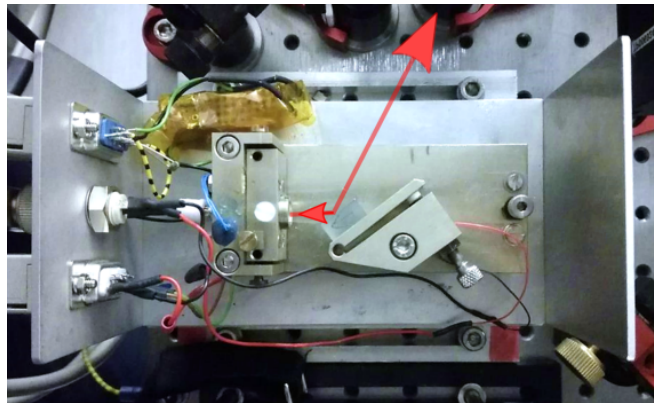


Figure 4.3: Self-built laser diode without its housing in the Littrow configuration. The red arrows indicate the beam path of the emitted light.

- **Laser diode:** The semiconductor laser diode from *Toptica Photonics* is placed in its mount. Its central wavelength is 920 nm. Through the adjustment of the grating the output wavelength is tuned to the D₁-transition of caesium at 894.52 nm.
- **Grating:** The holographic grating with 1200 lines/mm and a blaze angle of 36.52° was purchased from *Thorlabs*. It is glued to the grating mount. The angle of the grating defines the wavelength of the output beam. A fine thread screw in the grating mount allows for fine adjustments in the horizontal plane. The vertical

adjustment is done with another fine thread screw in the base plate and is tightened by two normal screws.

- **Piezoelectric transducer:** A small cylindrical piezoelectric transducer is set into the mount of the grating. The transducer fine tunes the wavelength of the output beam. Its position can be adjusted by a fine thread screw and by applying a voltage. The transducer is controlled by a proportional-integral-derivative (PID) controller and is a crucial component of the dichroic atomic vapour laser lock (DAVLL) system discussed in section 4.3.
- **Temperature control:** The temperature is constantly measured by a negative temperature coefficient (NTC) thermistor placed in the diode mount. The resistor is read out by a PID control built in in the ITC102 OEM laser diode and temperature controller from *Thorlabs*. A Peltier element beneath the baseplate is controlled by the PID and continually adjusts the temperature to a given value. The temperature is set to a constant value above room temperature.
- **Collimation lens and lens mount:** A collimation lens and its mount are placed in front of the diode laser. Through various screws its position is defined such that beam is collimated as good as possible.
- **Electronics and control:** The electric current of the laser diode and the Peltier element are controlled by the ITC102 from *Thorlabs*. A self-built protection circuit is set in front of the laser diode to protect it from current and voltage peaks.
- **Housing:** The housing consists of a base block to raise the laser diode to the working height of 10 cm and to serve as a heat sink. An additional cover plate shields the setup from dust, temperature gradients, and outside forces.

4.1.1 Fabry-Pérot cavity and mode hopping

To transform the time axis of the oscillator into a frequency axis and to compensate for a non-linear wavelength scan a Fabry-Pérot cavity is indispensable. The Fabry-Pérot cavity is an optical interferometer which consists of two parallel highly reflective mirrors with air in between. The transmission spectrum of the Fabry-Pérot shows high peaks at resonance frequencies of the interferometer. The spacing between the resonance frequencies is defined as the free spectral range - short FSR.

$$\nu_{\text{FSR}} = \frac{c}{2nL} \quad (4.1)$$

with the length between the mirrors L and the refractive index n equals 1. A Fabry-Pérot with a FSR of 331 MHz is part of the laser system of the signal laser. The Fabry-Pérot transmission spectrum furthermore allows one to check for a mode-hop free wavelength tuning range.

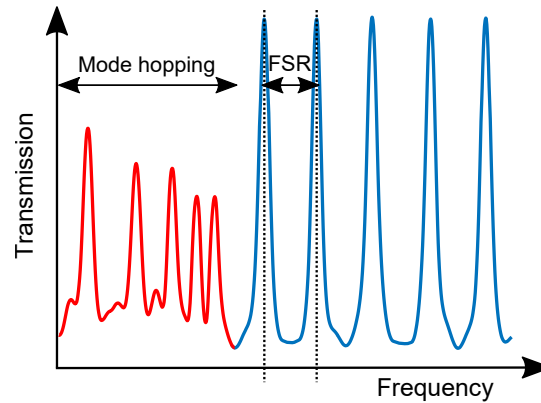


Figure 4.4: Transmission spectrum of the Fabry-Pérot with a red highlighted mode hopping regime.

Figure 4.4 shows a transmission spectrum of the Fabry-Pérot with the scanned signal laser. The mode hopping of the laser is highlighted in red. Mode hops are a transition between competing stable modes in the external cavity of the Littrow configuration or a stable multimode operation. The mode or the superposition of modes with the highest gain determines the output wavelength of the laser. Mode hops are unwanted in spectroscopy since it provokes a rapid change of the wavelength of the light to an undesirable wavelength range limiting the wavelength tuning.

Mode hops are caused by external influences such as temperature gradients, the detuning of the grating over a critical angle, or a change of the external cavity length. Internal effects such as a change of the pump power can also lead to mode hops. To minimize the risk of mode hopping, the fine adjustment of the self-built laser diode is checked regularly. Temperature stabilizing components and the optical table reducing external oscillations further minimise the risk of mode hopping.

4.2 DL Pro laser system

The DL Pro from *Toptica Photonics* is a grating stabilized diode laser. The DL Pro is controlled by the Sys DC 110, the diode laser supply electronics from *Toptica Photonics*. The Sys DC 110 provides the current for the DL Pro. It has an internal PID regulating the temperature of the laser. An external PID enables the feed forward function of the Sys DC 110, which stabilizes the laser system through an external DAVLL system as described in section 4.3. Table 4.1 summarizes the properties of the DL Pro.

4.3 Laser lock system

The lasers are locked to a transition through the DAVLL system - the dichroic atomic laser lock system. It stabilizes the output wavelength against the drifts caused by temperature

	Abbreviation	Value
Device		Stabilized diode laser
Device number		020664
Serial number		136555
Central wavelength	λ_0	895.0 nm
Output power	P_{out}	100.0 mW
Lasing threshold	I_{tres}	62 mA

Table 4.1: Properties of the DL Pro from *Toptica Photonics*. The values are taken from its datasheet.

gradients, mechanical fluctuations, or electronic variations. The schematic of the lock is shown in figure 4.5.

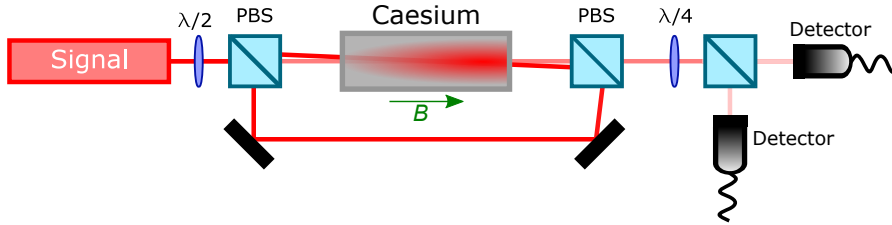


Figure 4.5: Schematic of the DAVLL setup. The laser wavelength is locked to an external reference provided through a saturation spectroscopy configuration. The magnetic field induced with a solenoid is depicted by the green arrow.

The signal field is scanned over the transition on which the laser is supposed to be locked. The signal beam is split into a low intensity probe beam and a high intensity coupling beam at a polarizing beam splitter. The beams are sent through the cell in a counter-propagating saturation spectroscopy scheme with which the lamp dips at the chosen transition are resolved. A magnetic field B implemented through a solenoid wrapped around the cell induces a Zeeman shift of the chosen transition. The circular polarizations σ^+ and σ^- are absorbed by different split up states with slightly shifted frequency to the original transition. A quarter-wave plate and a polarizing beam splitter separate the σ^+ and σ^- parts. Thus, they can be traced by two photodetectors separately. A differential amplifier subtracts the signals from each other creating an antisymmetric signal with a slope with zero-crossing at the frequency of the transition. A PID control can then process the signal for its feedback mechanism. It is connected to the piezoelectric transducer, which changes the wavelength accurately to compensate frequency drifts.

4.4 Electro-optical modulator - EOM

The electro-optical amplitude modulators used in this thesis were purchased from *Jenoptik* and are shown in figure 4.6 a). They are installed for the probe and the pump beam for

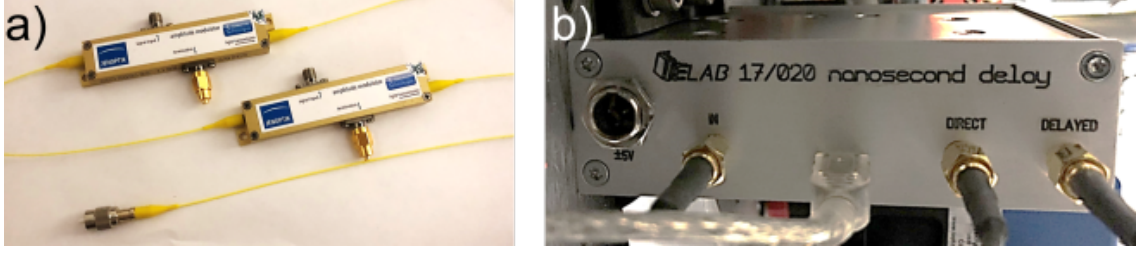


Figure 4.6: On the left is a photo of the fibre coupled EOMs from *Jenoptik*. The right picture shows the ELAB 17/020 nanosecond delay generator.

the future application in which the continuous wave lasers are chopped into short pulses and are used in the pulse propagation measurements to chop the signal field. Table 4.2 gives an overview of the properties of the EOMs.

	Abbreviation	Value
Device		amplitude modulator
Device number		AM905
Serial number		1500199-1168, 1500199-1169
Central wavelength	λ_0	905 nm
Insertion loss	D	5.1 dB
Extinction	E	43 dB
Half wave voltage at 1 kHz	V_π	2.76 V
Minimum optical rise time		~ 0.2 ns
Maximum input power	I_{\max}	100 mW cw

Table 4.2: Properties of the AM905 from *Jenoptik*. The values are taken from its data sheet.

Their function is described in [JEN]. As depicted in figure 4.7 a) the amplitude modulator consists of a Mach-Zehnder interferometer integrated in a waveguide. Light is coupled into the interferometer by polarization maintaining fibres. By applying a modulation voltage to the electrodes, the phase of the light is shifted. Interference effects lead to the change of the light amplitude. The interference fringes are depicted in figure 4.7 b). The extinction E is defined as

$$E = \frac{P_{out,max}}{P_{out,min}} \quad (4.2)$$

with the maximum $P_{out,max}$ and minimum $P_{out,min}$ output power.

The EOMs are controlled through a Matlab-script and the nanosecond delay generator ELAB17/020 assembled by the electronics workshop of the physical institutes of the university. The delay generator is shown in figure 4.6 b). The operation has been intensely studied in [Alb17]. The delay generator outputs an undelayed and a delayed voltage pulse with a maximum amplitude of 3 V and a rise time of about 1 ns. A delay from 15 to 50 ns

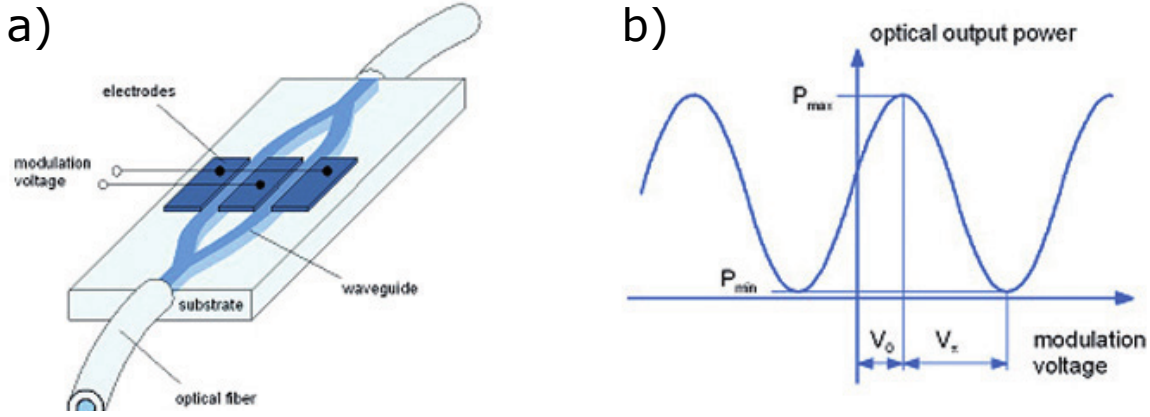


Figure 4.7: a) Schematic of the Mach-Zehnder waveguide structure. b) Output power as a function of the modulation voltage. [JEN]

can be adjusted in steps of 10 ps with the Matlab-script. The values were taken from the technical report published on the Physics-Elab website [Gri17].

The advantage of the EOMs over standard acousto-optic modulators (AOM) is the fast rise time. Their advantage over Pockels cells is the high extinction ratio and high repetition rate. However, the insertion loss D of 5.1 dB is high compared to typical values achieved with AOMs and Pockels cells. With a maximum input power $P_{in,max}$ of 100 mW the output power can maximally attain

$$P_{out,max} = P_{in,max} \cdot 10^{-D/10} = 30.903 \text{ mW}. \quad (4.3)$$

This is condoned due to the low background noise from the pump beam in the read-out process through the high extinction value. A tapered amplifier is increasing the signal after the EOM to amplify the intensity as described in section 4.5.

4.5 Tapered amplifier - TA

Tapered amplifiers are semiconductor-based optical amplifiers. The construction of the mount of the TA chip in the setup is based on the work by Jayampathi C. B. Kangara et al. [KHG⁺14].

Figure 4.8 shows the mount. The complete system consists out of the following components:

- **TA chip:** The TA chip was purchased from *Toptica Photonics*. The chip has an aperture of about $3 \mu\text{m}$ for coupling the seed laser into it and a wider aperture for emitting the amplified light.
- **Seed laser:** The DL Pro already discussed in section 4.2 is employed as the seed

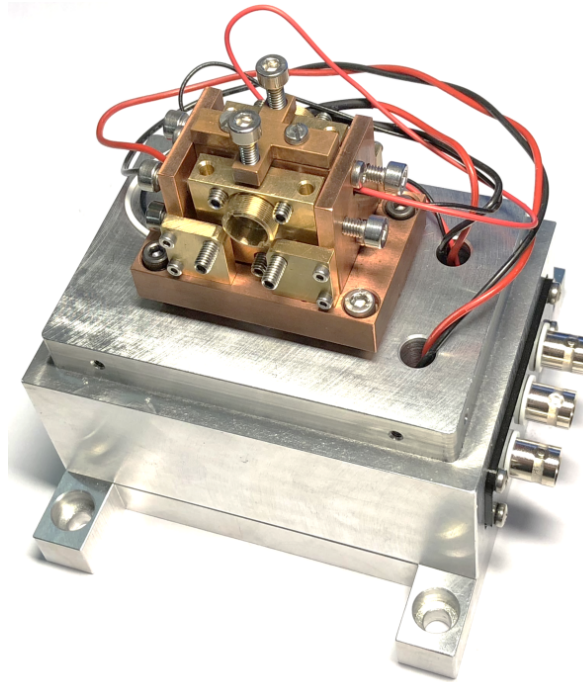


Figure 4.8: Self-built tapered amplifier mount including the temperature sensor, the TA chip and the Peltier element. The picture is taken without its housing. The design is based on [KHG⁺14].

laser. The beam has a diameter of $1000\ \mu\text{m}$. It is designed for an injection wavelength of $895\ \text{nm}$.

- Lenses and polarization optics:** An aspherical lens is used to couple into the waveguide structure of the chip. Another one is used to collimate the beam leaving the chip. To inject light into the chip, the seed laser should be mode matched with the chip. With a lens having a focal length of $11\ \text{mm}$ the beam is focused down to $3\ \mu\text{m}$. The polarization is matched with a half-wave plate. The output lens with a focal length of $3.75\ \text{mm}$ was adjusted in a way that the output beam is collimated in one axis.
- Mount:** The mount was fabricated by the mechanics workshop of the university. It is shown in figure 4.8. It consists of a copper mount for the TA chip in the center of the setup, mounts for two lenses, screws to adjust the position of the lenses and a housing to shield the system from temperature gradients, dust and other outside forces. The copper mount of the chip functions as the anode of the chip. It is both electrically and thermally conductive.
- Temperature stabilizing system:** The temperature sensor Hyg NTC-203 from *Reichelt* is built close to the chip. It is connected to the thermoelectric temperature controller TED200C from *Thorlabs*. The built-in PID-element controls a Peltier element located below the ground plate of the chip mount and above the heat sink

made out of aluminium. It is coated with a thin film of thermoconducting paste. The temperature is set to a constant value above room temperature.

4.5.1 Shaping the output beam

The output mode consists of multiple modes. These are shaped with four cylindrical lenses to collimate it and to create a beam shape as close to a Gaussian intensity distribution as possible. It is then coupled into a single mode fibre to obtain a single-mode beam for the experiments. Figure 4.9 shows the beam profile of the output beam after the beam shaping procedures. The picture was taken with a CCD camera. Interference fringes of the amplified spontaneous emission of the diode chip are visible.

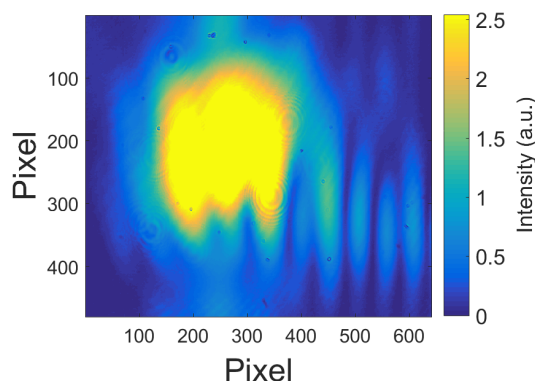


Figure 4.9: Beam profile of the output beam of the TA after the beam shaping optics.

4.6 Vapour cells

The measurements were done in cylindrical glass vapour cells. These cells are in a cell mount, which stabilizes the temperature through heating elements and provide a magnetic field via a solenoid if needed. By improving the design of the glass cells background light fields, coherence destroying processes, and signal losses can be suppressed. The following section expands on these topics.

4.6.1 Cell mount

The glass cells are located in self-built cell mounts. These provide steadiness, a constant temperature and a weak magnetic field if needed. The mount consists of the following components.

- **Housing blocks:** The cell is mounted in a holding between two aluminium blocks. They serve as a temperature reservoir to dampen the temperature fluctuations. The cell is clamped between the blocks.

- **Window clamp:** The copper clamp heats the cell windows. Its temperature can be adjusted by changing the voltage applied to the resistor screwed to the clamp. A hole in the clamp allows the light fields to enter and leave the cell. To prevent caesium to be deposited on the windows and create a reflective layer, the temperature is fixed around 25 °C above the temperature of the cell walls and the reservoir.
- **Solenoid:** The solenoid consists of a coated wire which surrounds the cylindrical cell. It provides a homogeneous magnetic field in the cell. The magnetic field is adjusted by the current and voltage of the electrical circuit connected to the solenoid.
- **Heating foil:** The cell walls are heated through a heating foil.

Figure 4.10 shows a picture of a cell in its mount without a solenoid.

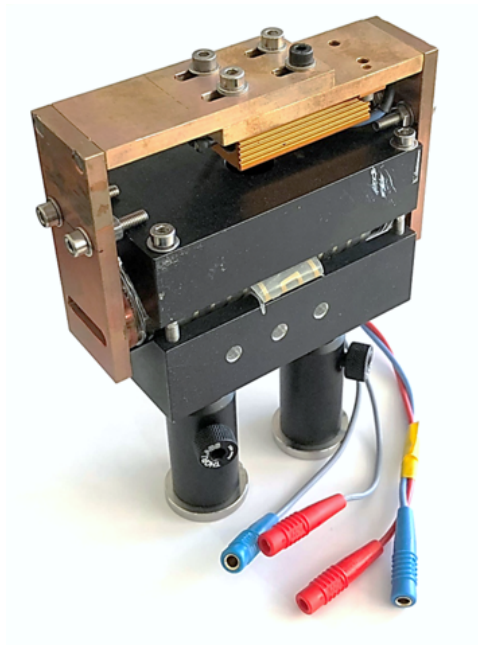


Figure 4.10: The self-built cell mount with a window clamp and heating foil.

4.6.2 Glass cell design

For increasing the storage times in future memory processes, the design of the vapour cells plays an important role. In the ideal case the cells meet the following demands:

1. The cell windows have constant or no birefringence to decrease the complexity of the experimental setup and to guarantee no spatially varying polarisation.
2. The windows have no reflections or absorption, which increases the read-out efficiency.

3. The cells have a paraffin coating to reduce the coherence loss caused by caesium-wall collisions.
4. A small window diameter reduces the risk of radiation trapping.
5. The cells are filled with neon or nitrogen buffer gases to increase the pump efficiency.

First steps were taken to realise these aims. The following subsection goes into the details of the fabrication.

Fabrication techniques

The glass windows are attached to their cylindrical counterpart by melting or glueing processes.

Melting the parts together is a well known fabrication method of the glass workshop of the university. Hereby, the glass parts are locally heated above the melting point of around $600\text{ }^{\circ}\text{C}$. Then, they are brought together before being cooled down to room temperature again. The process is repeated on the second side of the cell. To guarantee an even surface the heating is done while the glass parts are held in place and symmetrically rotated in the glass-working lathe depicted in figure 4.11. Then, the parts are put in an oven at around $450\text{ }^{\circ}\text{C}$. This so-called tempering process helps to reduce the induced stress of the material.



Figure 4.11: The glass-working lathe used in the glass workshop of the university. The burner softens the glass while it is rotated. This allows a symmetrical work on the cylindrical glass tubes.

Before glueing the cells, the parts are thoroughly cleaned. The glue, Epotek 301 from *Epoxy Technology*, is prepared according to the instructions. After applying it on the glass, it is heated on a heating plate at $100\text{ }^{\circ}\text{C}$ for approximately 30 minutes. The process is repeated on the other side. Afterwards, the glue is cured in an oven at $65\text{ }^{\circ}\text{C}$ for 2 hours.

After the production of the cells they are connected to a glass ampoule filled with caesium. Then, a pump reduces the air pressure inside the cells to about 10^{-7} bar. The seal is broken, the caesium fluidised through locally heating the glass structure and filled into the cell. Afterwards, the glass connection is melted and the cell is sealed air-tight. Figure 4.12 shows some cell designs.



Figure 4.12: Design of various cells. The two cells on the right are already closed and filled with caesium.

Advantages and disadvantages

The melting process needs high temperatures. The anti-reflective coating (AR coating), which is provided by *Thorlabs*, evaporates at around 250°C . Other coatings are not designed for higher temperatures, either. Creating the cells and providing an even window surface with an AR coating is not possible by melting the glass windows on the edges. Furthermore, the melting process induces high stress in the material. This leads to spatially varying refractive indices and thus to spatially dependent birefringence. Increasing the diameter of the windows does not improve the outcome. The stress in thinner windows is reduced, however the windows have to have a minimum thickness of around 1 mm to survive the tempering process. By tempering the cells, the stress is reduced.

Glueing cells does not need high temperatures and is not generating stress in the material. However, glue is outgassing. The process of releasing hydrogen and other gases into the cell creates a background gas disturbing and overshadowing the spectroscopic measurements. Former attempts in the group have shown, that glued cells without buffer gases are not a suitable solution for long-term usage in measurements and data reproducibility.

Glued cells with buffer gases might make them suitable and should be investigated in a subsequent work for a better understanding.

Anodic bonding, glass frit bonding, or optical bonding techniques may be a better solution for the fabrication of the cells. They work with lower temperatures hence, will not affect the AR coating. They provide an air-tight contact which is not influenced by the highly reactive caesium and provide a manageable complexity. However, these fabrication techniques are not available with the current equipment.

	Experience	Temperature	Stress	Outgassing
Melting	high	high	high	very low
Glueing	high	low	low	very high
Bonding	low	medium	?	very low

Table 4.3: Overview of the advantages and disadvantages of the different fabrication mechanisms

Table 4.3 gives an overview of the advantages and disadvantages of the fabrication methods. The work presented in this thesis was done with the well-known glass cells created by melting the pieces together without any coatings. They have a cell length of 7.5 cm and a diameter of 3 cm.

5 Measurements

This chapter will focus on the measurements. The aim is to characterize the EIT signal, induce a broad transparency window, and measure pulse deformation as a function of the coupling Rabi frequency. A broad transparency window renders the storage of broadband photons possible allowing an insensitive and steady operation, independent of laser fluctuations. In addition, it would allow hybrid setups with quantum dots which emit photons with a bandwidth of more than 1.2 GHz.

The measurements were done with a constant coupling light field. With a better knowledge of the coherence disrupting processes, background light fields, high detection efficiencies, and a perfect control of time sequences storage protocols are doable in the current setup. The intended improvements are summarized in chapter 6. The counter-propagating scheme as depicted in figure 4.1 promises less radiation background through the on-resonant four-wave mixing background discussed in section 3.3.1. The unwanted light is emitted in the direction of the coupling light field and filtered out, easily. The co-propagating assembly will be introduced first to serve as a basis for the comparison of both schemes.

The measurements were done in the same caesium vapour cell with 7.5 cm length and 3 cm diameter. It is a melted glass cell without coatings. The optical density of the cell is calculated by a fitting procedure analogous to [SAGH08], which fits the absorption spectrum of the cell. The measurements are done at room temperature and the optical density as defined in section 3.4.1 is 0.603.

5.1 Co-propagating EIT scheme

In the co-propagating scheme coupling and signal light fields have the same direction of propagation. As shown in figure 3.5 the EIT feature is expected to be steep and narrow. The measured transmission spectrum is described by the intensity function $I(z)$ as defined in section 3.4.1.

$$I(z) = I_0 e^{ikz\chi/2} \quad (5.1)$$

Figure 5.1 shows the measured transmission spectrum dependent on the coupling Rabi frequency. The absorption is correlated to the imaginary part of the susceptibility according to equation 5.1. The absorption is normalized to the transition from $6^2S_{1/2}$ F=3 to $6^2P_{1/2}$ F=4. The detuning represents the detuning from resonance. The hyperfine transition from $6^2S_{1/2}$ F=3 to $6^2P_{1/2}$ F=3 is addressed as well leading to a second absorption profile. With increasing coupling Rabi frequency the feature gets more prominent and

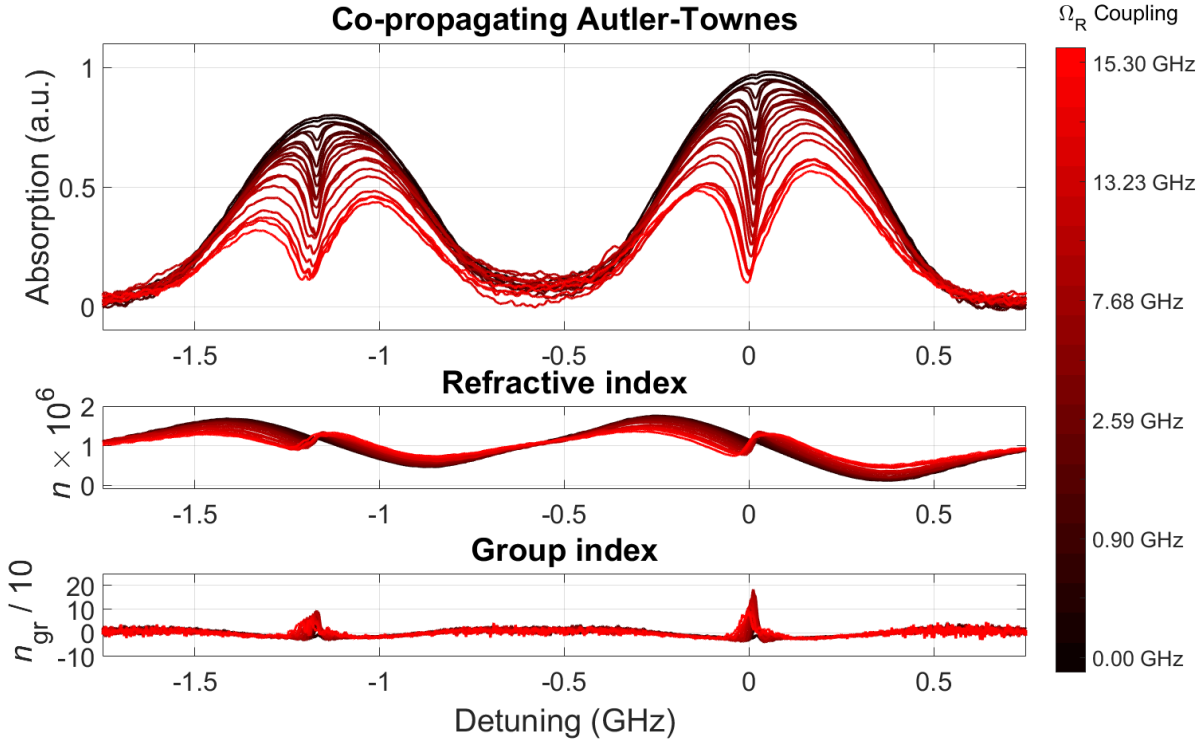


Figure 5.1: Co-propagating Autler-Townes splitting as a function of the coupling Rabi frequency Ω_R . $\Delta = 0$ denotes the $6^2S_{1/2}$ $F=3$ to $6^2P_{1/2}$ $F=4$ transition. The refractive index is calculated via equation 3.2 from the absorption spectrum. The group index is simulated according to equation 3.39.

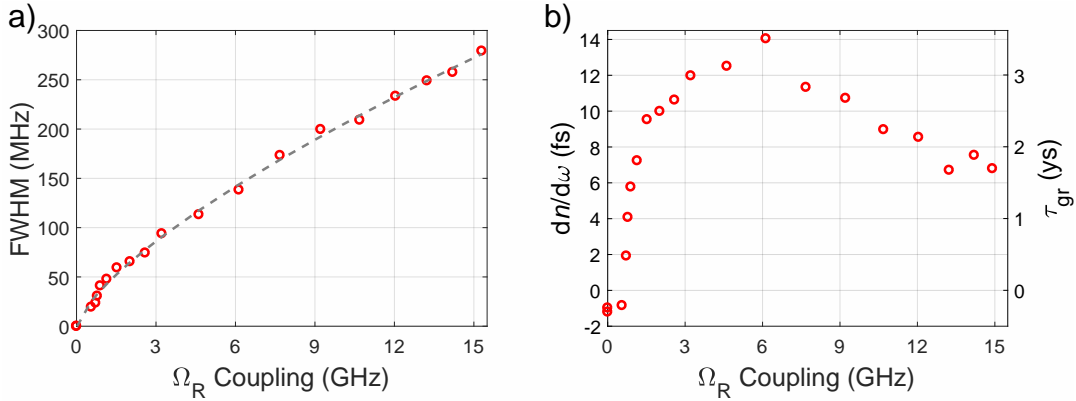


Figure 5.2: a) The full width at half maximum of the absorption spectrum in figure 5.1. The dotted line is merely a guide for the eye. b) The derivative of the refractive index with respect to its angular frequency ω . The second axis defines the group delay in 10^{-24} s with a cell length of 7.5 cm as defined by equation 5.3.

more deep, decreasing the absorption and increasing the transparency of the medium for the signal field. Through absorption effects, the edges of the EIT feature get washed out.

The full width at half maximum (FWHM) of the feature is characterised in figure 5.2 a). Hereby, the FWHM is the width of the difference of the absorption profile at the resonant transition without a coupling field and the profile with a coupling field. With increasing coupling power the width increases.

As defined in section 3.2.1 the refractive index is

$$n_{\text{gr}} = n(\omega) + \omega \frac{\partial n}{\partial \omega} \approx 1 + \frac{1}{2} \chi' \quad (5.2)$$

for weakly absorbing media. Through a Kramers-Kronig transformation of the measured imaginary part of the susceptibility the real part including the dispersive properties of the medium is derived. The refractive index corresponding to the absorption spectrum is plotted beneath it. As expected, the refractive index has a steep positive slope at the minimum of the EIT feature. Figure 5.2 illustrates its dependence on the coupling light field. Until around 4.5 GHz the derivative of the refractive index with respect to its angular frequency rises. For higher coupling light fields the derivative decreases again.

The group index n_{gr} is derived from the refractive index. It is a measure for the delay which propagating light suffers according to equation 3.40.

$$\tau_{\text{gr}} = L \left(\frac{1}{v_{\text{gr}}} - \frac{1}{c} \right) = \frac{L}{c} n_{\text{gr}}. \quad (5.3)$$

With increasing group index the delay increases proportionally. Since the group index is proportional to the derivative of the refractive index with respect to its angular frequency, the group index has a maximum at the centre of the EIT feature. This relationship is harnessed in slow light experiments. The third graph of figure 5.1 shows the calculated group index of the absorption spectrum in the first graph. With increasing coupling Rabi frequency the feature at 0-detuning rises. Around 4.5 GHz the feature decreases in height again. For a cell length of 7.5 cm the on-resonant group delays for the spectrum in figure 5.1 have values up to 3.51 ys.

Figure 5.3 shows the simulated absorption spectrum of a three-level lambda scheme in caesium for the D₁ transition. The Doppler effect and absorption of the coupling light field according to [Sid14] are taken into account. The simulation confirms the observation of the measurements.

5.2 Counter-propagating EIT scheme

Through a minor adjustment in the setup, the measurements were redone in a counter-propagating scheme. The counter-propagating scheme promises lower radiation background from four-wave mixing and an easy separation of probe and coupling light fields.

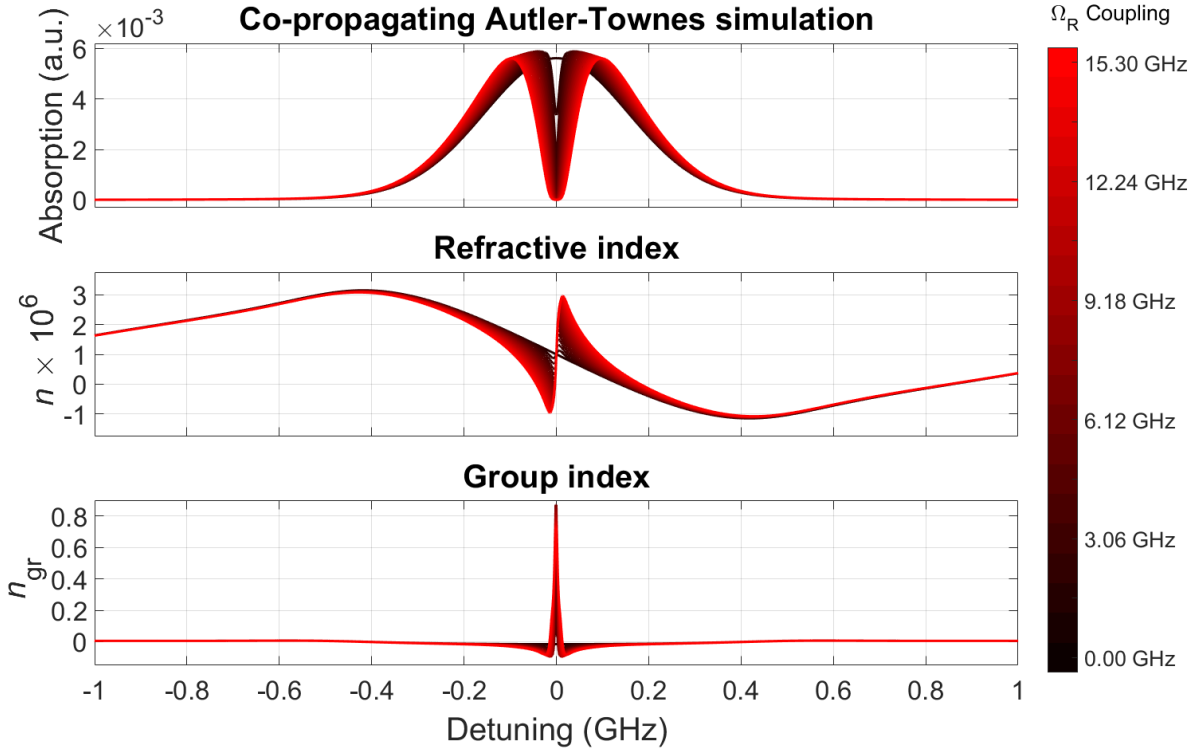


Figure 5.3: Simulation of the co-propagating Autler-Townes splitting. 0 denotes the $6^2S_{1/2}$ to $6^2P_{1/2}$ transition. The probe Rabi frequency is 10 MHz. The coupling Rabi frequency is varied. The coupling light field decreases with the cell length as a function of the absorption coefficient as described by [Sid14].

However, as shown in figure 3.5 the EIT feature is not expected to be as definite as the feature in a co-propagating scheme.

The counter-propagating absorption spectrum is shown in figure 5.4. The EIT feature is not as distinctive as the feature in the co-propagating scheme. By comparing figures 5.5 and 5.2 a) it is clearly seen that the width of the feature is broader in the counter-propagating scheme. A broad transparency window is desired since it allows the capability to store light with large bandwidths and to be insensitive to frequency fluctuations in storage protocols.

Since all velocity classes are addressed, the edges of the feature get flattened. This leads to lower values of the derivative of the refractive index with respect to the angular frequency at resonance. While the FWHM of the co-propagating scheme is roughly $3/4$ of the FWHM of the counter-propagating value, the derivative is more than twelve times higher than the derivative in the counter-propagating scheme.

The group index shown in the third graph in figure 5.4 is thus not as distinctive and only about half as high as in the co-propagating case. Therefore, delays and storage protocols will not work as efficiently in the counter-propagating scheme. The counter-propagating

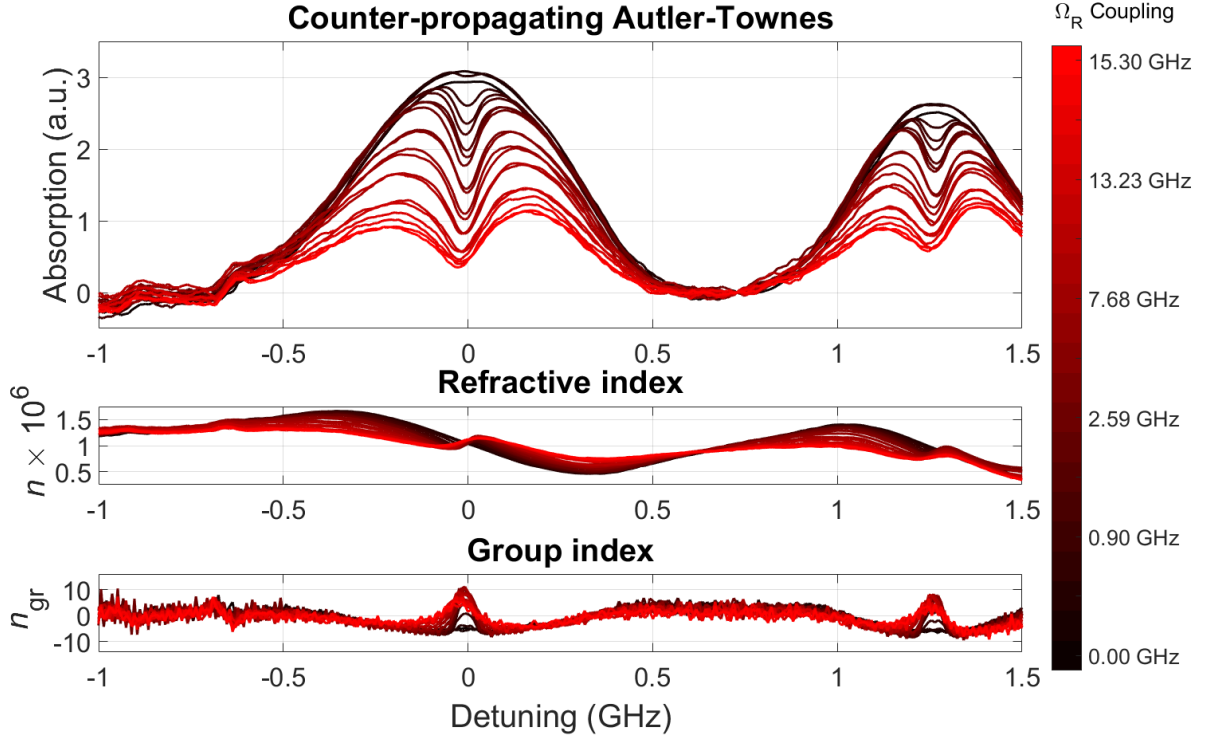


Figure 5.4: Counter-propagating Autler-Townes splitting. 0 detuning denotes the $6^2S_{1/2}$ $F=3$ to $6^2P_{1/2}$ $F=4$ transition. The refractive index is calculated analogous to equation 3.2. The group index is simulated according to equation 3.39.

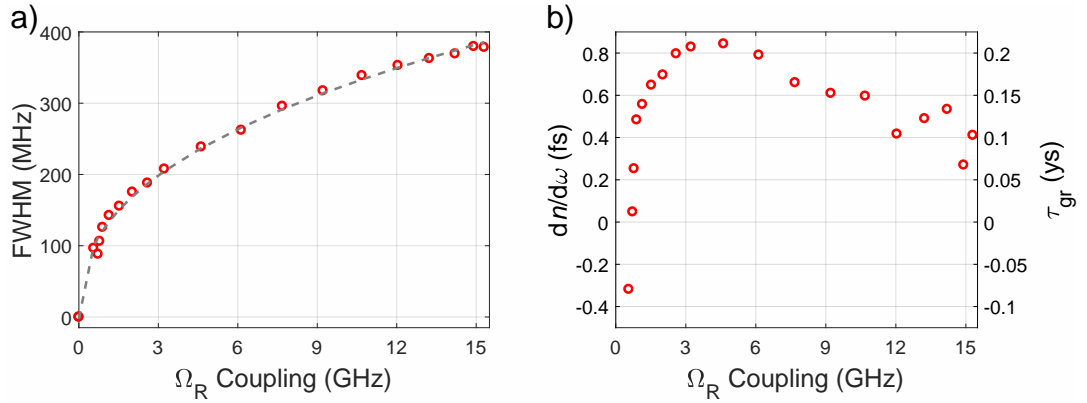


Figure 5.5: a) The full width at half maximum of the absorption spectrum in figure 5.4. The dotted line is merely a guide for the eye. b) The derivative of the refractive index with respect to its angular frequency. The axis on the right specifies the group delay in 10^{-24} s according to equation 5.3 with a cell length of 7.5 cm.

direction of the beams is however indispensable, since the on-resonant background can not be filtered out with neither optical nor temporal means.

Storage processes need a time dependent sequence as described in section 3.3. The time dependence is introduced in pulse propagation measurements in the following section.

5.3 Pulse deformation

In this section, the pulse deformation dependency of a constant on-resonant coupling Rabi frequency is investigated. Hereby, the signal field is chopped with the EOM described in section 4.4.

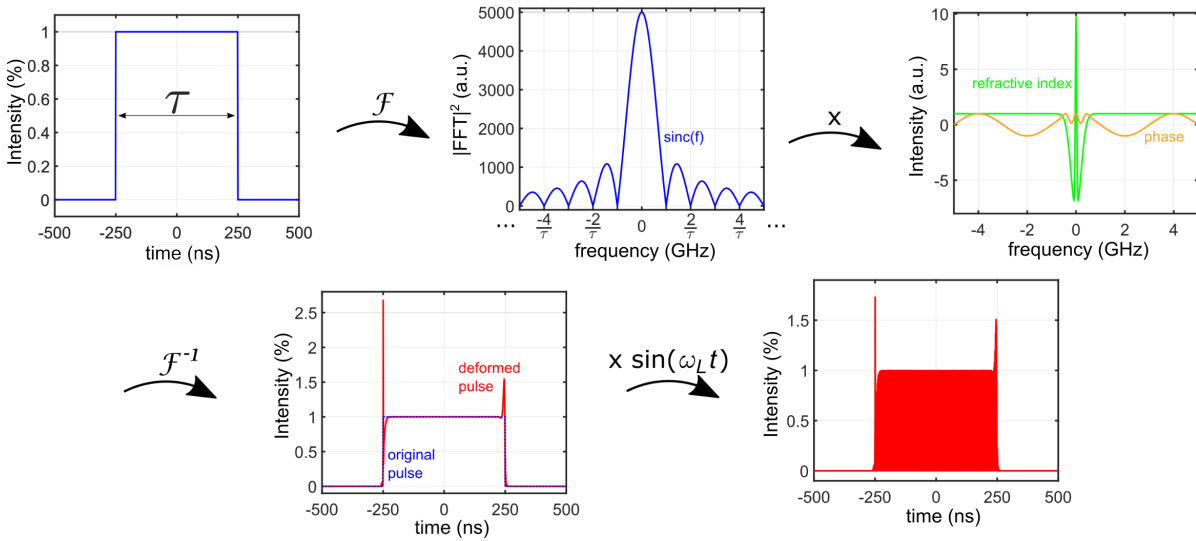


Figure 5.6: Depiction of the calculation steps taken for simulating the behaviour of a pulse propagating through caesium vapour. It is deformed through the dispersion of the refractive index with a resonant coupling light field with a Rabi frequency of 4.6 GHz. The refractive index is approximated by a fit to measured data. The depicted refractive index is a fit to the data from the counter-propagating scheme.

The propagating pulse undergoes a frequency dependent phase shift. The impact of the phase shift on the pulse is simulated as follows. The sequence is illustrated in figure 5.6.

1. A rectangular pulse with width τ and height 1 is created.
2. A Fourier transform decomposes the pulse into its frequencies. The frequency components are described by a sinc function.
3. In the frequency domain the sinc function is multiplied by an additional phase ϕ which is caused by the dispersion of the refractive index. The refractive index is approximated by a second order Gaussian fit to the data from figure 5.4 for

the counter-propagating scheme and from figure 5.1 for the co-propagating scheme with a coupling Rabi frequency of 4.6 GHz. The phase is defined by

$$\phi = e^{-ikz} = e^{-iz \cdot n\omega/c}. \quad (5.4)$$

4. Subsequently, the function is inversely transformed to receive the pulse with its deformations.
5. To get the light signal the transformed signal is multiplied with $\sin(\omega_L t)$. Here, ω_L is the frequency of the light. For better clarity only the envelope is considered in the following.

With the convolution theorem and the associativity with a scalar multiplication it can be shown that the oscillation with ω_L does not have to be included in the Fourier transformation. The Fourier transformation of the function $\sin(\omega_L t) \cdot \text{rect}(\tau, t)$ multiplied with the phase ϕ can be written as

$$\begin{aligned} \mathcal{F}\{\sin(\omega_L t) \cdot \text{rect}(\tau, t)\} \cdot \phi &= (\mathcal{F}\{\sin(\omega_L t)\} * \mathcal{F}\{\text{rect}(\tau, t)\}) \cdot \phi \\ &= \mathcal{F}\{\sin(\omega_L t)\} * (\mathcal{F}\{\text{rect}(\tau, t)\} \cdot \phi). \end{aligned} \quad (5.5)$$

\mathcal{F} denotes the Fourier transform, $\text{rect}(\tau, t)$ the rectangular function with width τ and height 1 and $*$ is the mathematical operation of the convolution. The inverse transformation yields

$$\mathcal{F}^{-1}\{\mathcal{F}\{\sin(\omega_L t)\} * (\mathcal{F}\{\text{rect}(\tau, t)\} \cdot \phi)\} = \sin(\omega_L t) \cdot (\mathcal{F}^{-1}\{\mathcal{F}\{\text{rect}(\tau, t)\}\} \cdot \phi). \quad (5.6)$$

It is thus sufficient not to include the light oscillation in the Fourier transform.

Figure 5.7 shows the deformation of pulses with various pulse lengths in a co- and counter-propagating scheme. The schemes are differed by the approximated refractive index. The blue pulse is the original undeformed reference pulse and is filled with blue for better visibility. The area below the deformed pulse is the same as the area of the undeformed pulse since losses have not been included in the simulation.

The slowly rising left edge of the deformed pulses in the co-propagating scheme is as expected. Absorption effects dominate the early-arriving light fields until the system arrives at steady state. A rapid increase at the rising edge of the deformed pulses in the counter-propagating scheme physically does not make sense since absorptions effects dominate the first part of an arriving pulse. The very thin peaks are most likely due to the confined frequency domain in the simulation. Since the feature is very narrow, high frequency components seem to be weighted more as they should. The absorbed photons of the early-arriving light increases the emission of light at the lately-arriving edge of the pulses.

Figure 5.8 shows the measured pulses with five different pulse widths and five different coupling Rabi frequencies. The blue pulses are the reference pulses which were measured

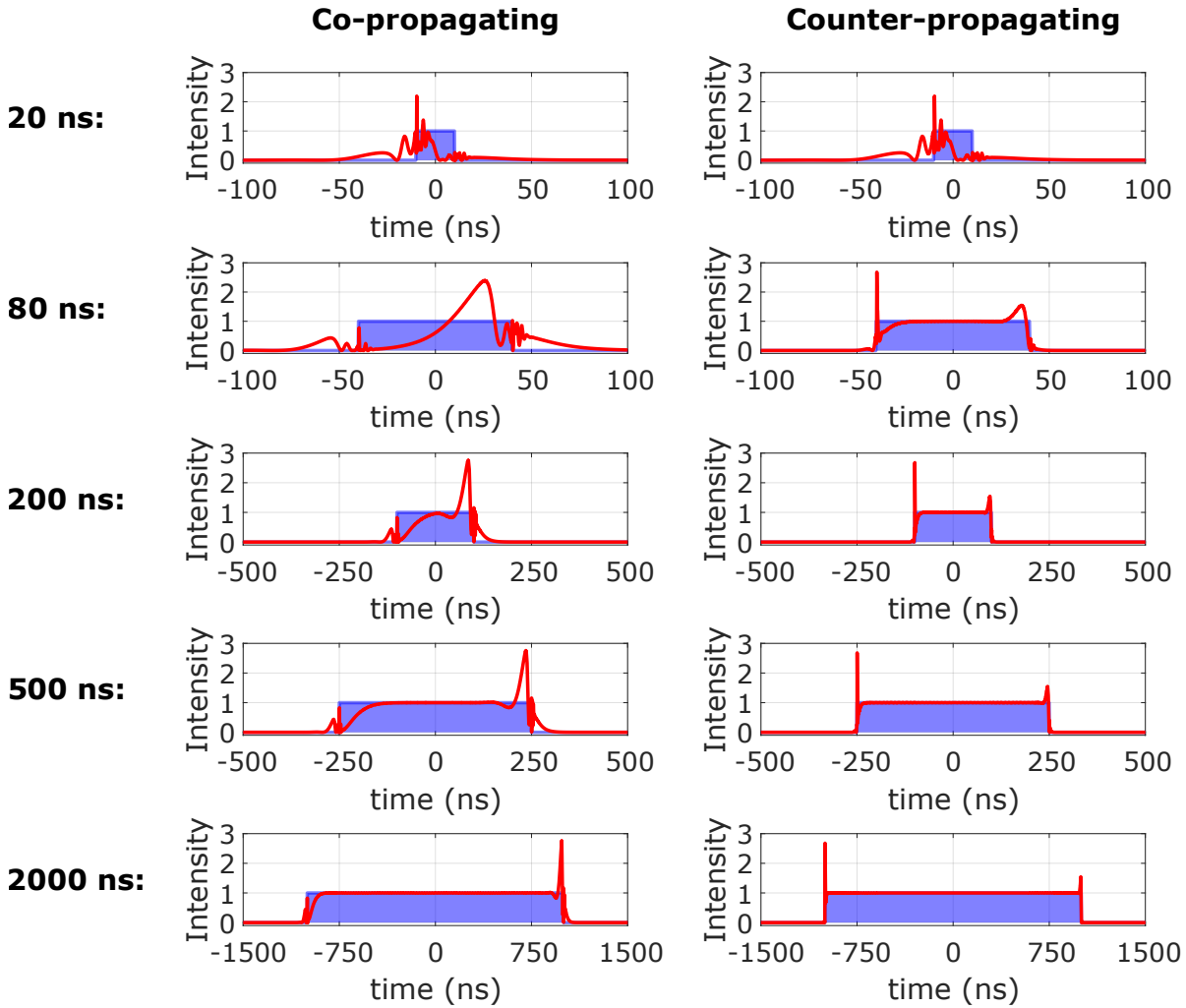


Figure 5.7: Simulation of the pulse deformation through the dispersion of the refractive index. The simulation was done according to the protocol described by figure 5.6. The blue rectangular signal is the original pulse without deformation. It is shadowed with blue for better visibility. Negative times refer to the early-arriving part of the pulses on a detector. Positive times indicate the lately-arriving components.

with a very far detuned off-resonant frequency and without a coupling light field. The pulses were measured in a counter-propagating scheme. The intensity was manually set to 0 for the first hundred data points.

The data was taken with the PDA10A-EC - Si switchable gain detector from *Thorlabs*. The detector has a bandwidth of 150 MHz. To increase the resolution of the detector the input impedance of the oscillator was set to $50\ \Omega$. The slowly rising edges of the pulses with a 20 ns pulse width indicate that these arrangements however did not suffice to resolve it. The oscillations after the falling edge of the pulses with a pulse width of 20, 80 and 200 ns are most probably due to overshoots of the electronics and don't carry

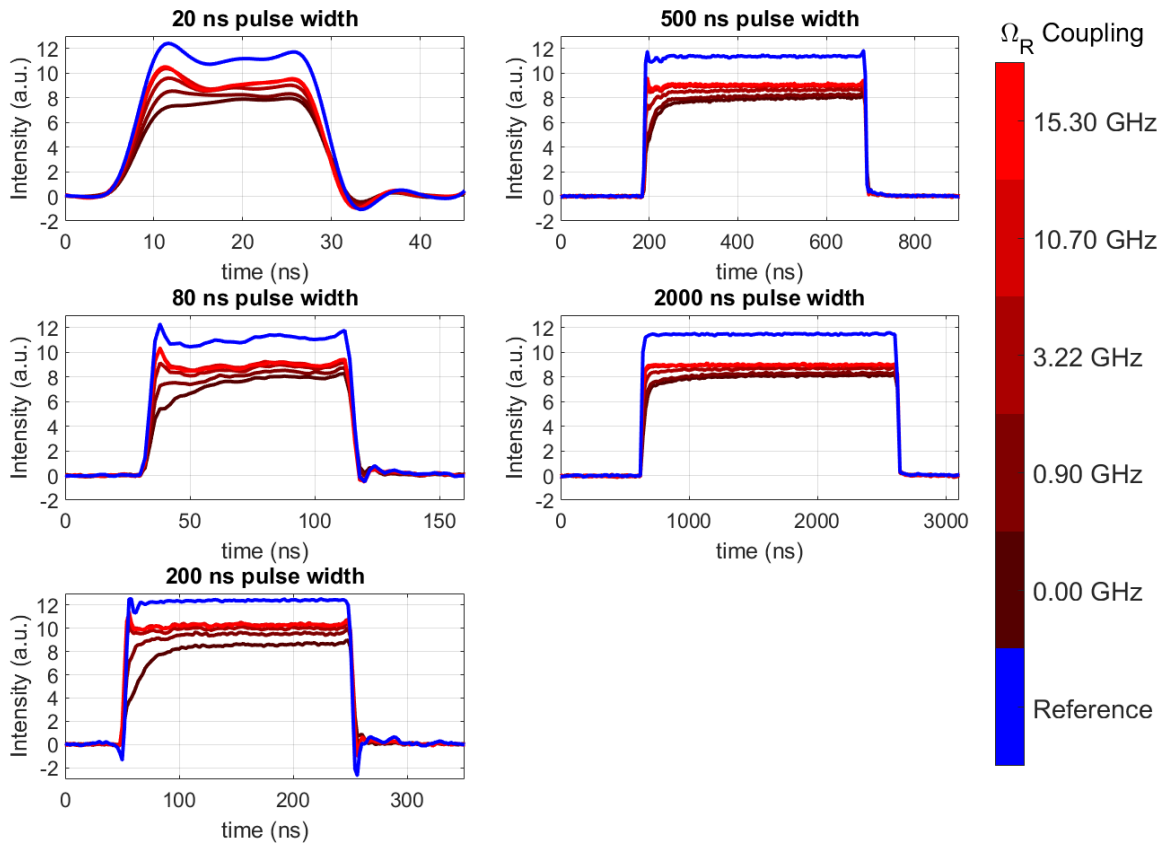


Figure 5.8: The deformation of pulses after the interaction with caesium as a function of the coupling Rabi frequency Ω_R . Pulse widths of 20, 80, 200, 500 and 2000 ns were measured. The blue pulses are reference pulses recorded with very far detuned signal frequency and without the coupling laser.

any physical meaning.

The slowly rising left edge of the pulses is similar to the expected pulse envelope of the simulation. The light intensities of the pulses approach a constant value as predicted. However, the intensities do not reach the same values. The pulses with high Rabi frequencies reach higher values as a consequence of the induced transparency through the coupling light field. An additional background light field induced by it cannot be ruled out. An increased intensity at the falling edge similar to the simulation is not visible.

The pulse propagation measurements have shown the possibility to analyse and create time dependent processes. Further increasing the sensitivity of the setup through faster detection components will however be indispensable for first slow light measurements. Intended improvements are discussed in the following chapter.

6 Outlook

Quantum memories have the potential to enhance entanglement distribution protocols to a point at which large-scale entanglement distributing networks are reliable and feasible. Functional quantum repeaters will enable secure communication through quantum cryptographic protocols such as the quantum key distribution. Quantum technologies will profit from the better knowledge and control of single photons and entangled photon pairs.

First large-scale networks distributing entangled states and proving quantum teleportation have been realised by sending single photons to a satellite [YRL⁺12] [YCL⁺17]. Atmospheric turbulences limit the reliability and are difficult to overcome through prediction. Large-scale networks through optical fibres have the potential to be more insusceptible provided with trustworthy quantum memories.

This work lays the basis for an implementation of quantum memories in hot caesium vapour cells. The setup is the fundament for future protocols which allow a continuous-wave or pulsed operation of the lasers and an easy replacement of them through fibre couplers for a single-photon source. For realising single-photon storage the setup will have to overcome the limitations introduced in section 3.3.1. Intended improvements for the current setup are presented in the following.

6.1 The lambda scheme

Improving the lambda scheme as introduced in this thesis will reduce the background to enable single-photon storage processes.

- **Temporal post-selection:** A well-understood process will allow temporal post-selection. Only a time window in which a read-out photon is to be expected will be considered.
- **Filtering system:** The filtering system will have to be able to detect single photons and reduce the noise and the background light level to a minimum. Through a short pass filter the off-resonant light will be filtered out. Getting rid of the on-resonant light through radiation trapping or four-wave mixing will however be challenging. Polarization optics, the counter-propagating scheme and a spatial tilt of the beams will further reduce the background. They will however also limit the storage efficiency. A suitable trade-off has to be found. Etalon filters and cavities placed around the cell will further reduce the background. Since the on-resonant

four-wave mixing is emitted in the same direction as the stored photon it will be impossible to completely filter it out.

- **Hybrid system with quantum dots:** In cooperation with the *Institut für Halbleitertechnik und Funktionelle Grenzflächen, Universität Stuttgart* the signal laser used in this thesis will be replaced by a quantum dot emitting single photons at the wavelength of the caesium $6^2S_{1/2}$ to $6^2P_{1/2}$ transmission. The frequency spectrum of 1.2 GHz bandwidth will greatly limit the read-out efficiency due to high photon losses. It will nevertheless prove the concept until further improvements through the extended lambda scheme introduced in the following section will be realised.
- **Vapour cells:** The currently not possible bonding processes will be further investigated. An AR coating and a paraffin coating will improve the measurements as described in section 4.6. Improving the cell design will need further knowledge of the impact of buffer gases. Neon, nitrogen or a mixture of both might reduce undesirable coherence destroying effects and thus increase the possible storage time.
- **Magnetic shielding:** Magnetic stray field gradients disrupt the coherence of the caesium ground states by shifting the energy levels out of resonance. Magnetic μ -metal shielding will greatly reduce the source of error and increase the efficiency. This improvement is however not as crucial for the reliability of storage processes as the previously introduced enhancements.

6.2 The extended lambda scheme

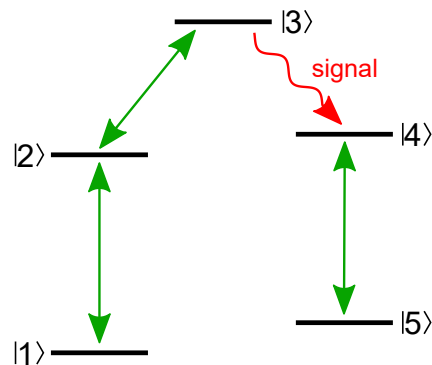


Figure 6.1: The extended lambda scheme. The transitions depicted in green will be driven by pulsed lasers. The transition of the to be stored signal is depicted in red.

An extended lambda scheme as depicted in figure 6.1 will overcome the filtering challenges of the three-level lambda scheme. Alkali atoms provide an adequate level structure to realise it. Furthermore, the two upper transitions in a scheme in caesium or rubidium can be chosen to be in the telecom wavelength of around 1550 nm. This is favourable

for the implementation of quantum memories, since the widely spread glass fibres have an absorption minimum at the telecom wavelength and which is the most widely used wavelength in current optical networks.

Through three pulsed lasers depicted in green, the red to be stored signal resonant to the $|3\rangle$ to $|4\rangle$ transition will be mapped onto a collective spin-wave excitation of states $|1\rangle$ and $|5\rangle$. This scheme will overcome the four-wave mixing background since the pulsed operation provides population in the upper energy levels only in the storage process. Background radiation will be easily filtered out, since it is off-resonant. The same holds for radiation trapping.

Further simulations and experiments will contribute to a better understanding of the processes and are planned for the near future in a subsequent work.

7 Summary and conclusion

This work lays the fundament for future single-photon storage protocols in caesium vapour cells. A low-maintenance, applicable, and efficient quantum memory would enable quantum repeaters which are a crucial component of large-scale quantum networks as described in chapter 2.

In an EIT storage scheme the control of the transparency of a medium is harnessed. By opening a transparency window and closing it as soon as the signal is in the media, light is mapped onto a collective spin wave excitation. By inducing transparency by a read-out pulse subsequently, the signal can be read out.

The experimental setup introduced in chapter 4 fulfils various requirements needed for future storage processes. The laser systems are frequency locked and stable. They can be arranged in a counter- and co-propagating three-level lambda scheme in caesium. The light fields can be temporally controlled through two EOMs and a delay generator. First steps were taken to improve the vapour cells and thus extend the ground state coherence time. A longer coherence time will allow longer storage times of the single photons since coherence destroying processes destruct the spin wave excitation.

The functionality of the setup has been shown in EIT and pulse propagation measurements in chapter 5. The EIT measurements show the possibility of a controllable transparency in the caesium vapour. By adapting the coupling Rabi frequency the EIT feature grows or decreases in depths and widens or narrows. In agreement with the theory, the feature is narrow and deep in a co-propagating scheme and broad and flat in a counter-propagating scheme. The advantages of the counter-propagating scheme compared to a co-propagating alignment is the absence of a disruptive four-wave mixing background which can not be filtered out. Furthermore, a broader transparency window resulting in a storage process insusceptible to frequency fluctuations and able to handle single photons with a broad frequency spectrum is possible in this scheme. However, the efficiency is limited by the shallow EIT feature which leads to lower group indices. Pulse propagation dependent on a coupling light field in a counter-propagating scheme have been analysed for a better understanding of time-dependent processes. Simulation and measurements are in agreement.

Further improving the setup as described in chapter 6 with an extended lambda scheme will elude the difficulties of the counter-propagating three-level scheme enabling single-photon measurements.

8 Acknowledgement

In this chapter I want to express my gratefulness to those people without whom this work would not have been possible.

First of all, I want to thank Prof. Dr. Tilman Pfau for giving me the opportunity to do my masters thesis at the PI5. My gratitude is extended to Prof. Dr. Jörg Wrachtrup for being the second examiner.

I would like to express my appreciation to my supervisor Robert Löw for his helpful advice, guidance, patience and proof reading.

I thank Harald Kübler for always finding the time to support me in experimental and theoretical issues.

I want to acknowledge the help given by Fabian Ripka, Hao Zhang, Patrick Kaspar, Florian Christaller, Annika Belz and Maxim Leyzner through enlightening discussions, their assisting attitude and pleasant working atmosphere. I am grateful to Hadiseh Alaeian for the quick proof reading and assistance. My special thanks are extended to the 3rd floor, the other institute and the secretary members for sharing their experience, their friendly spirit and for sparing me a lot of trouble.

Technical support given by Frank Schreiber has been a great help in working on the vapour cells.

I am grateful for the capable counselling concerning the quantum dots and the many enjoyable discussions with Simone Luca Portalupi and Hüseyin Vural from the IHFG. I value the opportunity to visit the laboratory and gain an impression of the difficulties with which they have to deal.

I appreciate Lena Engel, Ana Çutuk, Philipp Tatar-Mathes, Abdelhamid Ameer, Lyane-Antonin Mavoungou and Bernd Röslin for the great time we had while studying physics, for the cohesion and the many hours playing card games.

Finally, I want to thank my family and friends who have always backed me up.

List of References

- [Alb17] Ralf Albrecht. Integrated and time-resolved measurements of collisional energy transfer in rubidium p-states. Master's thesis, 5. Physikalisches Institut, Universität Stuttgart, December 2017. (page 33)
- [ALSM06] Annabel L. Alexander, Jevon J. Longdell, Matthew J. Sellars, and Neil B. Manson. Photon echoes produced by switching electric fields. *Phys. Rev. Lett.*, 96:043602, February 2006. (page 6)
- [AUA⁺10] Mikael Afzelius, Imam Usmani, Atia Amari, Björn Lauritzen, Andreas Walther, Christoph Simon, Nicolas Sangouard, Jiří Minář, Hugues de Riedmatten, Nicolas Gisin, and Stefan Kröll. Demonstration of atomic frequency comb memory for light with spin-wave storage. *Phys. Rev. Lett.*, 104:040503, January 2010. (page 6)
- [BEK⁺17] Matthias Bock, Pascal Eich, Stephan Kucera, Matthias Kreis, Andreas Lenhard, Christoph Becher, and Jürgen Eschner. High-fidelity entanglement between a trapped ion and a telecom photon via quantum frequency conversion. *ArXiv e-prints*, October 2017. (page 5)
- [Bet16] Robert J. Bettles. *Cooperative Interactions in Lattices of Atomic Dipoles*. PhD thesis, Durham University, 2016. (page 9)
- [Blo03] Immanuel Bloch. Licht-Atom Wechselwirkung im Zwei-Niveau System. Course notes, December 2003. (page 9)
- [BVS15] Klaas Bergmann, Nikolay V. Vitanov, and Bruce W. Shore. Perspective: Stimulated Raman adiabatic passage: The status after 25 years. *Journal of Chemical Physics*, 142(17):170901, May 2015. (page 20)
- [CLM⁺14] Eric Chitambar, Debbie Leung, Laura Mančinska, Maris Ozols, and Andreas Winter. Everything You Always Wanted to Know About LOCC (But Were Afraid to Ask). *Communications in Mathematical Physics*, 328:303–326, May 2014. (page 4)
- [Dem11] Wolfgang Demtröder. *Laserspektroskopie 1*. Springer-Verlag, 6 edition, 2011. (page 24, 25, 27)
- [Dem13] Wolfgang Demtröder. *Laserspektroskopie 2*. Springer Spektrum, 6 edition, 2013. (page 24)

- [DiV00] David P. DiVincenzo. The physical implementation of quantum computation. *Fortschritte der Physik*, 48(9-11):771–783, 2000. (page 1)
- [DLCZ01] Lu-Ming Duan, Mikhail Lukin, Ignacio Cirac, and Peter Zoller. Long-distance quantum communication with atomic ensembles and linear optics. *Nature*, 414:413–418, November 2001. (page 4)
- [Eri12] Wesley W. Erickson. *Electromagnetically Induced Transparency*. Bachelor’s thesis, Reed College, 2012. (page 13, 15)
- [FIM05] Michael Fleischhauer, Atac Imamoglu, and Jonathan P. Marangos. Electromagnetically induced transparency: Optics in coherent media. *Rev. Mod. Phys.*, 77:633–673, July 2005. (page 13, 14, 15, 18)
- [Gri17] Axel Griesmaier. Nanosecond delay generator. techreport, Physics ELab, 2017. (page 34)
- [HHDB99] Lene V. Hau, Stephen E. Harris, Zachary Dutton, and Cyrus H. Behroozi. Light speed reduction to 17 metres per second in an ultracold atomic gas. *Nature*, 397:594–598, February 1999. (page 17)
- [HHS⁺08] Gabriel Hétet, Mahdi Hosseini, Ben M. Sparkes, Daniel Oblak, Ping K. Lam, and Ben C. Buchler. Photon echoes generated by reversing magnetic field gradients in a rubidium vapor. *Opt. Lett.*, 33(20):2323–2325, October 2008. (page 6)
- [JEN] JENOPTIK Optical Systems GmbH, Goeschwitzer Strasse 25; 07745 Jena. *Integrated-optical modulators, Technical information and instructions for use*. www.jenoptik.com/light-modulators. (page 33, 34, 60)
- [JSC⁺04] Brian Julsgaard, Jacob Sherson, J. Ignacio Cirac, Jaromír Fiurášek, and Eugene S. Polzik. Experimental demonstration of quantum memory for light. *Nature*, 432:482–486, November 2004. (page 6)
- [KHG⁺14] Jayampathi C. B. Kangara, Andrew J. Hachtel, Matthew C. Gillette, Jason T. Barkeloo, Ethan R. Clements, Samir Bali, Brett E. Unks, Nicholas A. Proite, Deniz D. Yavuz, Paul J. Martin, Jeremy J. Thorn, and Daniel A. Steck. Design and construction of cost-effective tapered amplifier systems for laser cooling and trapping experiments. *American Journal of Physics*, 82(8):805–817, 2014. (page 34, 35, 60)
- [Kim08] Harry J. Kimble. The quantum internet. *Nature*, 453:1023, June 2008. (page 3, 4, 59)
- [KXCK17] Fumihiro Kaneda, Feihu Xu, Joseph Chapman, and Paul G. Kwiat. Quantum-memory-assisted multi-photon generation for efficient quantum information processing. *Optica*, 4(9):1034–1037, September 2017. (page 5, 6, 59)

-
- [LDBH01] Chien Liu, Zachary Dutton, Cyrus H. Behroozi, and Lene V. Hau. Observation of coherent optical information storage in an atomic medium using halted light pulses. *Nature*, 409:490–493, 2001. (page 6)
- [LFSM05] Jevon J. Longdell, Elliot Fraval, Matthew J. Sellars, and Neil B. Manson. Stopped light with storage times greater than one second using electromagnetically induced transparency in a solid. *Phys. Rev. Lett.*, 95:063601, August 2005. (page 6)
- [LST09] Alexander I. Lvovsky, Barry C. Sanders, and Wolfgang Tittle. Optical quantum memory. *Nature Photonics*, 3:706–714, 2009. (page 4, 5)
- [NC10] Michael A. Nielsen and Isaac L. Chuang. *Quantum computation and quantum information*. Cambridge University Press, Cambridge [u.a.], 10th anniversary ed. edition, 2010. (page 1)
- [Ott11] Johannes S. Otterbach. *Single- and Many-Body Phenomena of Dark-State Polaritons*. PhD thesis, Technische Universität Kaiserslautern, October 2011. (page 18)
- [Rei11] Klaus F. Reim. *Broadband optical quantum memory*. PhD thesis, University of Oxford, 2011. (page 6, 21)
- [SAGH08] Paul Siddons, Charles S. Adams, Chang Ge, and Ifan G. Hughes. Absolute absorption on rubidium d lines: comparison between theory and experiment. *Journal of Physics B: Atomic, Molecular and Optical Physics*, 41(15):155004, 2008. (page 41)
- [SEDF17] Slava Smartsev, David Eger, Nir Davidson, and Ofer Firstenberg. Continuous generation of delayed light. *Journal of Physics B: Atomic, Molecular and Optical Physics*, 50(21):215003, 2017. (page 6)
- [Sid14] Paul Siddons. Light propagation through atomic vapours. *Journal of Physics B: Atomic, Molecular and Optical Physics*, 47(9):093001, 2014. (page 24, 43, 44, 61)
- [SNH96] Jon Sagle, Raychel K. Namiotka, and John Huennekens. Measurement and modelling of intensity dependent absorption and transit relaxation on the cesium d1 line. *Journal of Physics B*, 29(12):2629, 1996. (page 22)
- [ST08] Bahaa E. A. Saleh and Malvin C. Teich. *Grundlagen der Photonik*. Lehrbuch Physik. Wiley-VCH, Weinheim, 2., vollst. überarb. und erw. Aufl. edition, 2008. (page 8)
- [Ste10] Daniel A. Steck. Cesium d line data, December 2010. (page 7, 8, 25, 59)

- [TMK⁺17] Sarah E. Thomas, Joseph H. D. Munns, Krzysztof T. Kaczmarek, Cheng Qiu, Benjamin Brecht, Amir Feizpour, Patrick M. Ledingham, Ian A. Walmsley, Joshua Nunn, and Dylan J. Saunders. High efficiency raman memory by suppressing radiation trapping. *New Journal of Physics*, 19(6):063034, 2017. (page 20, 22, 23)
- [VGL98] Jacques Vanier, Aldo Godone, and Filippo Levi. Coherent population trapping in cesium: Dark lines and coherent microwave emission. *Phys. Rev. A*, 58:2345–2358, September 1998. (page 21)
- [WBH⁺17] Janik Wolters, Gianni Buser, Andrew Horsley, Lucas Béguin, Andreas Jöckel, Jan-Philipp Jahn, Richard J. Warburton, and Philipp Treutlein. Simple atomic quantum memory suitable for semiconductor quantum dot single photons. *Phys. Rev. Lett.*, 119:060502, August 2017. (page 6, 20)
- [YCL⁺17] Juan Yin, Yuan Cao, Yu-Huai Li, Sheng-Kai Liao, Liang Zhang, Ji-Gang Ren, Wen-Qi Cai, Wei-Yue Liu, Bo Li, Hui Dai, Guang-Bing Li, Qi-Ming Lu, Yun-Hong Gong, Yu Xu, Shuang-Lin Li, Feng-Zhi Li, Ya-Yun Yin, Zi-Qing Jiang, Ming Li, Jian-Jun Jia, Ge Ren, Dong He, Yi-Lin Zhou, Xiao-Xiang Zhang, Na Wang, Xiang Chang, Zhen-Cai Zhu, Nai-Le Liu, Yu-Ao Chen, Chao-Yang Lu, Rong Shu, Cheng-Zhi Peng, Jian-Yu Wang, and Jian-Wei Pan. Satellite-based entanglement distribution over 1200 kilometers. *Science*, 356(6343):1140–1144, 2017. (page 50)
- [YRL⁺12] Juan Yin, Ji-Gang Ren, He Lu, Yuan Cao, Hai-Lin Yong, Yu-Ping Wu, Chang Liu, Sheng-Kai Liao, Fei Zhou, Yan Jiang, Xin-Dong Cai, Ping Xu, Ge-Sheng Pan, Jian-Jun Jia, Yong-Mei Huang, Hao Yin, Jian-Yu Wang, Yu-Ao Chen, Cheng-Zhi Peng, and Jian-Wei Pan. Quantum teleportation and entanglement distribution over 100-kilometre free-space channels. *Nature*, 488:185–188, 2012. (page 50)
- [ZZHE93] Marek Żukowski, Anton Zeilinger, Michael A. Horne, and Artur K. Ekert. “Event-ready-detectors” Bell experiment via entanglement swapping. *Phys. Rev. Lett.*, 71:4287–4290, December 1993. (page 4, 59)

List of Figures

2.1	Basic components of quantum networks. A photon is generated, sent through a channel, “amplified” in a quantum repeater and distributed to the end nodes where they are processed [Kim08].	3
2.2	Entanglement swapping scheme as described in [ZZHE93]. “QMeas.” is the abbreviation for quantum measurement.	4
2.3	Scheme of the ring cavity introduced in [KXCK17]. Incoming photons are stored in the cavity until the polarization is switched by the Pockels cell (PC) allowing the transmittance through the polarizing beam splitter (PBS).	6
3.1	a) Energy levels of the caesium D_1 transition. b) The corresponding spectrum with lamb dips. The values are from [Ste10].	8
3.2	Schematics of a two-level atomic system consisting of the ground state $ g\rangle$ and an excited state $ e\rangle$	9
3.3	Schematic of a three-level scheme consisting of two ground states $ 1\rangle$ and $ 2\rangle$, and an excited state $ 3\rangle$. The red arrow denotes the probe field ω_p . The blue arrow indicates the coupling light fields. The decays are depicted in green.	13
3.4	Real and imaginary parts of the susceptibility in a three-level system. The real part describes the absorption, the imaginary part describes the dispersive behaviour. In a) the line shapes are shown without the coupling laser. In b) the coupling Rabi frequency Ω_c equals $0.5/\gamma_{31}$. There is no decay between states $ 1\rangle$ and $ 2\rangle$	16
3.5	The EIT feature dependency on counter or co-propagating probe and coupling light fields. In a) and b) the velocity classes as a function of the probe detuning are plotted. The colour bar visualizes the value of the population. In c) and d) the population is summed up over all velocity classes leading to the familiar EIT feature for the counter-propagating case. In a co-propagating scheme the feature vanishes.	17
3.6	a) EIT feature versus probe and coupling laser detuning. Lighter colors refer to higher values of χ'' . b) χ'' for different coupling powers.	17
3.7	The imaginary part of the susceptibility of an EIT feature with $\Omega_c = 10\Omega_p$, $\gamma_{21} = 0.02$ Hz, γ_{31} the natural decay rate of the $6^2S_{1/2}$ to $6^2P_{1/2}$ transition in caesium and its corresponding refractive index n and group index n_{gr}	18
3.8	Group index n_{gr} for various coupling Rabi frequencies. With decreasing Rabi frequency the group index at resonance increases.	18

3.9 a) Laser sequences of the storage process and b) its corresponding lambda level scheme. The indices s and c refer to the signal and coupling fields, respectively. The times t_1 and t'_1 denote the time in which the write and signal fields are sent into the cell, respectively. They share the same value in a off resonant Raman scheme. In an on resonant stimulated Raman adiabatic passage (STIRAP) scheme t'_1 is slightly delayed as depicted in a). 20

3.10 Scheme of the signal pulse compression and broadening through a caesium vapour cell dependent on the group velocity v_{gr} for a frequency independent refractive index. 23

3.11 Four-wave mixing scheme. The strong signal field creates an artificial state through which the population is transferred from state $|1\rangle$ to state $|2\rangle$ by an additional Stokes transition denoted by α 24

4.1 Schematics of the experimental setup. The blue colour of the laser beam was merely chosen to differentiate between coupling and signal beam. The fibres are polarisation maintaining fibres. Beam shaping optics are not included for better clarity. 28

4.2 Schematic of the Littrow configuration. α denotes the diffraction angle. LD is the abbreviation of laser diode. The Littrow configuration stabilizes the laser diode, narrows its linewidth, and enables the tuning of the wavelength to a certain value. 29

4.3 Self-built laser diode without its housing in the Littrow configuration. The red arrows indicate the beam path of the emitted light. 29

4.4 Transmission spectrum of the Fabry-Pérot with a red highlighted mode hopping regime. 31

4.5 Schematic of the DAVLL setup. The laser wavelength is locked to an external reference provided through a saturation spectroscopy configuration. The magnetic field induced with a solenoid is depicted by the green arrow. 32

4.6 On the left is a photo of the fibre coupled EOMs from *Jenoptik*. The right picture shows the ELab 17/020 nanosecond delay generator. 33

4.7 a) Schematic of the Mach-Zehnder waveguide structure. b) Output power as a function of the modulation voltage. [JEN] 34

4.8 Self-built tapered amplifier mount including the temperature sensor, the TA chip and the Peltier element. The picture is taken without its housing. The design is based on [KHG⁺14]. 35

4.9 Beam profile of the output beam of the TA after the beam shaping optics. 36

4.10 The self-built cell mount with a window clamp and heating foil. 37

4.11 The glass-working lathe used in the glass workshop of the university. The burner softens the glass while it is rotated. This allows a symmetrical work on the cylindrical glass tubes. 38

4.12 Design of various cells. The two cells on the right are already closed and filled with caesium. 39

5.1	Co-propagating Autler-Townes splitting as a function of the coupling Rabi frequency Ω_R . $\Delta = 0$ denotes the $6^2S_{1/2}$ F=3 to $6^2P_{1/2}$ F=4 transition. The refractive index is calculated via equation 3.2 from the absorption spectrum. The group index is simulated according to equation 3.39.	42
5.2	a) The full width at half maximum of the absorption spectrum in figure 5.1. The dotted line is merely a guide for the eye. b) The derivative of the refractive index with respect to its angular frequency ω . The second axis defines the group delay in 10^{-24} s with a cell length of 7.5 cm as defined by equation 5.3.	42
5.3	Simulation of the co-propagating Autler-Townes splitting. 0 denotes the $6^2S_{1/2}$ to $6^2P_{1/2}$ transition. The probe Rabi frequency is 10 MHz. The coupling Rabi frequency is varied. The coupling light field decreases with the cell length as a function of the absorption coefficient as described by [Sid14].	44
5.4	Counter-propagating Autler-Townes splitting. 0 detuning denotes the $6^2S_{1/2}$ F=3 to $6^2P_{1/2}$ F=4 transition. The refractive index is calculated analogous to equation 3.2. The group index is simulated according to equation 3.39.	45
5.5	a) The full width at half maximum of the absorption spectrum in figure 5.4. The dotted line is merely a guide for the eye. b) The derivative of the refractive index with respect to its angular frequency. The axis on the right the specifies the group delay in 10^{-24} s according to equation 5.3 with a cell length of 7.5 cm.	45
5.6	Depiction of the calculation steps taken for simulating the behaviour of a pulse propagating through caesium vapour. It is deformed through the dispersion of the refractive index with a resonant coupling light field with a Rabi frequency of 4.6 GHz. The refractive index is approximated by a fit to measured data. The depicted refractive index is a fit to the data from the counter-propagating scheme.	46
5.7	Simulation of the pulse deformation through the dispersion of the refractive index. The simulation was done according to the protocol described by figure 5.6. The blue rectangular signal is the original pulse without deformation. It is shadowed with blue for better visibility. Negative times refer to the early-arriving part of the pulses on a detector. Positive times indicate the lately-arriving components.	48
5.8	The deformation of pulses after the interaction with caesium as a function of the coupling Rabi frequency Ω_R . Pulse widths of 20, 80, 200, 500 and 2000 ns were measured. The blue pulses are reference pulses recorded with very far detuned signal frequency and without the coupling laser.	49
6.1	The extended lambda scheme. The transitions depicted in green will be driven by pulsed lasers. The transition of the to be stored signal is depicted in red.	51